NANO · MICRO small
www.small-journal.com

Enhancing the Chemical Reactivity of Graphene through Substrate Engineering

*Jia Tu and Mingdi Yan**

Covalent functionalization of pristine graphene can modify its properties, enabling applications in optoelectronics, biomedical fields, environmental science, and energy. However, the chemical reactivity of pristine graphene is relatively low, and as such, methods have been developed to increase the reactivity of graphene. This review focuses on substrate engineering as an effective strategy to enhance the reactivity of graphene through strain and charge doping. Nanoparticles, metals with different crystal orientations, and stretchable polymers are employed to introduce strains in graphene, leading to enhanced chemical reactivity and increased degree of functionalization. Charge doping through orbital hybridization with metals and charge puddles induced by oxide substrates generally enhance the reactivity of graphene, while alkyl-modified surfaces and 2D materials often reduce graphene reactivity via charge screening and van der Waals interactions that increase the stability of the graphene layer, respectively. This review summarizes methods for creating and characterizing strains and charge doping in graphene and discusses their effects on the chemical functionalization of graphene in various reactions.

1. Introduction

Graphene is a 2D nanomaterial having exclusive sp^2-hybridized carbons arranged in a hexagonal lattice. It has exceptional properties such as high strength, conductivity, and transparency.[1] Pristine graphene can be considered as a gigantic aromatic molecule, which results in low chemical reactivity. Its zero bandgap, while beneficial for applications requiring high conductivity and rapid electron mobility such as transparent conductive electrodes[2] and high-frequency devices,[3] can limit its utility in other applications like electronic switching devices.[3] Covalent functionalization modifies the properties of graphene,[4–13] including introducing new functionalities on graphene and tuning its conductivity and the bandgap.[13–16] Functionalized graphene has found utilities in optoelectronics, medical devices, environmental sensing and purification, and energy storage.[4,9–11] Due to its low reactivity, graphene typically undergoes reactions involving reactive intermediates such as free radicals, nitrenes, carbenes, or arynes, or requires harsh conditions such as oxidation, hydrogenation, or halogenation. Various methods have been developed to enhance the reactivity of graphene, including by applying electric field[17–19] or external force,[20] antaratopic addition or ditopic addition,[21–23] by creating nanomesh or defects on graphene,[24–28] by utilizing the graphene stacking mode,[29–31] or by controlling the number of graphene layers.[32–37]

Pristine graphene is a delicate, flat sheet that is prone to mechanical damage, often requiring substrate support for stability, ease of handling, and to prevent wrinkling or deformation.[38] Common substrates used to support graphene, including semiconductors, metals, polymers, and oxides, can interact with graphene in ways that can affect its electronic, mechanical, and chemical properties.[39] For example, the number of graphene layers grown by chemical vapor deposition (CVD) can be controlled by using different metal substrates; the charge transport and current flow in graphene can be altered through the formation of Schottky junctions with semiconductors at the interface; dielectric ceramics can be used as substrates to influence both the electronic and mechanical properties of graphene.[39–43] Graphene supported on substrates has also been used in catalyzing various reactions.[44–50]

Substrates on which graphene is supported can also significantly influence the chemical reactivity of graphene. Through substrate engineering and by introducing strain and/or charge doping in graphene, the reactivity and degree of functionalization can be enhanced. Common methods to create strain include using nanoparticle-decorated substrates, specific crystal orientations of metal substrates, or mechanically deforming polymer substrates. Generally, tensile strain is produced when the graphene sheet is stretched, whereas compressive strain is generated when the graphene sheet is compressed. First-principles calculations showed that a 1% uniaxial tensile strain could open a bandgap of ≈300 meV, with the bandgap increasing almost

J. Tu, M. Yan
Department of Chemistry
University of Massachusetts Lowell
Lowell, MA 01854, USA
E-mail: mingdi_yan@uml.edu

The ORCID identification number(s) for the author(s) of this article can be found under https://doi.org/10.1002/smll.202408116

DOI: 10.1002/smll.202408116

linearly with strain.[51] This tunability offers a mechanism to tune the bandgap of graphene through applied strain.

Charge doping occurs when graphene is placed on a substrate that either donates or withdraws electrons. When charge doping is introduced in graphene, it shifts the Fermi level and modifies the band structure.[52] In the case of *n*-type or electron doping, the Fermi level shifts above the Dirac point, bringing it closer to the conduction band. This increases the electron density in graphene, making it more reactive toward electrophiles. In the case of *p*-type or hole doping, the Fermi level shifts below the Dirac point, bringing it closer to the valence band. This increases the hole density in graphene, making it more reactive toward nucleophiles. Charge doping can either increase or decrease the reactivity of graphene, depending on the nature and the type of reaction. Strongly interacting metals such as Ni and oxides such as SiO_2 and Al_2O_3 generally increase the reactivity of graphene. Substrates that decrease the reactivity of graphene include 2D materials which increase the stability of graphene through van der Waals (vdW) forces, and self-assembled monolayers (SAMs) which screen charges on the substrate.

In the sections below, we discuss the origins of strains and charge doping in graphene, methods to characterize these effects. We summarize the literature examples on how strain and charge doping have been effectively used to enhance the reactivity and degree of functionalization of graphene. For readers interested in the impact of chemical functionalization on the electronic and other properties of supported graphene, we refer to the recent review by Prato and coworkers, which also provided a comprehensive overview of covalent modifications, particularly radical reactions, for substrate-supported graphene and other 2D materials.[5]

2. Effect of Strain on the Reactivity of Graphene

2.1. Strain in Graphene

The effect of strain can be illustrated by comparing the structure and reactivity of graphene with its closely related carbon materials of carbon nanotubes and fullerenes. The low reactivity of pristine graphene is due to its highly conjugated and planar structure where the π electrons are delocalized over the entire graphene sheet. Carbon nanotubes and fullerenes also contain conjugated sp^2 carbon atoms, but these structures are non-planar. When the planar sp^2 structure curves, the carbon atoms must bend out of the plane. This bending, or pyramidalization, increases the *s*-character in the π bonds. As a result, the π electrons become less delocalized, making the bent carbon atoms more chemically reactive compared to those in the planar graphene.[53] Therefore, an effective way to increase the reactivity of graphene is to distort it from its planar structure, which can be achieved by introducing strain.

Solid substrates are particularly useful in this regard as their surfaces are typically not perfectly flat and can naturally induce strain in the graphene layer. Strain can be generated through surface topography of the substrate, which produces wrinkles, ripples, and local curvature in graphene. Even for the atomically flat material such as mica, the root mean square (RMS) roughness is ≈0.05 nm.[54] The interaction between graphene and the substrate tends to lower the energy of the system, causing graphene to conform to surface features of the substrate.[55,56] This conformal adhesion to the substrate deviates graphene from its ideal flat configuration, thus introducing strains in graphene. Silicon wafers, which are single crystal silicon covered by a surface layer of either thermally grown or native silicon dioxide layer, are the most technologically important substrates in microelectronics and device fabrication.[57] Graphene conforms well on silicon wafers. Film thickness of graphene on silicon wafer measured by scanning tunneling microscopy (STM) was 4.2 Å in vacuum, which is comparable to the layer spacing of 3.4 Å in graphite, and 9 Å in air, with the excess height being attributed to the presence of gas species (air or moisture) between graphene and silicon wafer and/or adsorbed on the graphene sheet.[38] Graphene supported on silicon wafer is reported to be slightly smoother than the silicon wafer itself, with the measured RMS roughness of 0.35 and 0.37 nm, respectively.[58] Furthermore, it has been reported that graphene could reproduce ≈99% of the topography of silicon wafers including the smallest features, indicating that the observed roughness is extrinsic, caused by the substrate, rather than an intrinsic property of graphene.[38,58] This high-fidelity conformation of graphene to the substrate suggests that substrates can be effective for creating strain in graphene. For example, graphene fabricated by mechanical exfoliation on silicon wafers or transferred to silicon wafers has shown to be under in-plane stress of −0.2–0.4%.[59] In this case, the tensile strain has been suggested to be more likely than compressive strain due to buckling along the out-of-plane direction. Thermal annealing can relieve this strain at 100 °C or convert the tensile strain to compressive strain at higher temperatures.[59]

While native substrates can induce some strain in graphene due to surface imperfections and inherent roughness, they usually cause small or modest perturbations and produce relatively low levels of strain. To achieve higher strains in graphene, additional methods have been developed. In this review, we discussed examples where the reactivity of graphene has been enhanced by strains created through nanoparticles, metal lattice structures, and mechanical deformation of polymers. Other methods have also been used to increase strains in graphene, including using nanopillars[60–63] or nanotrenches[64] to create mechanical stress and deformations in the graphene layer, through thermal expansion and contraction,[59] and using patterned elastomeric stamps to induce controlled folds in graphene.[65] These examples have not been followed up with testing the reactivity of graphene and are therefore not included in this review. Nevertheless, these methods are valuable to explore in the context of graphene reactivity.

2.2. Characterization of Strain in Graphene

Raman spectroscopy is the most used technique for the characterization of graphene, including the strain in graphene and interactions of graphene with substrates.[51,59,66–72] Monolayer pristine graphene has two main characteristic Raman peaks: The G peak ≈1580 cm^{-1} and the 2D peak ≈2690 cm^{-1} at 532 nm laser excitation and is a prominent feature of graphitic materials. The D peak ≈1350 cm^{-1} is absent in defect-free graphene due to crystal symmetry but appears when there are defects in graphene such as physical defects or when chemical functionalization of graphene

converts sp^2 to sp^3 carbons. The intensity of the G peak, however, is proportional to the number of sp^2 C atoms in graphene and can be considered as a constant at low defect density. Under this condition, the intensity ratio of D peak and G peak, I_D/I_G, increases with increasing concentration of sp^3 carbons, and has been widely used to characterize the extent of functionalization in graphene including the majority of examples in this review.[73] The D′ peak, which is a defect-induced scattering at ≈1620 cm^{-1}, can also appear in the Raman spectrum of functionalized graphene.

Tensile strain typically shifts the Raman peaks to lower frequencies.[51] This was reasoned as due to the decreased carbon-carbon bond strength in graphene under tensile strain when the bonds within the graphene lattice are stretched.[51] On the other hand, compressive strain shifts the Raman peaks to higher frequencies. When a large tension or compression is applied to graphene, the G peak can split into two components: G^+ and G^-,[66,68] but in the context of chemical reactions on graphene, the strain is relatively small and such splitting is not obvious. Several studies mentioned the shift of G band and 2D band as a function of strain, but the extent of shift varies, possibly due to different methods for strain generation or the presence of additional effects.[69] For example, Ni et al. reported significant redshifts in the Raman 2D band (27.8 cm^{-1} per 1% strain) and G band (14.2 cm^{-1} per 1% strain).[51] Yu et al. quantified the sensitivity of the 2D band frequency to tensile strain as -7.8 cm^{-1}/%.[72] In both studies, strains were generated using a polyester substrate, with the former by unidirectional stretching while the latter by bending.

A recently developed vector model has gain increasing use for characterizing strain and charge doping in graphene by Raman spectroscopy.[59,67–69] The model was built from results collected from multiple strained and charge-doped samples. The Raman 2D band frequency (ω_{2D}) was plotted against the G band frequency (ω_G), and the results were compared to the freestanding graphene without strain or doping. Freestanding graphene can be prepared by suspending graphene on an open well or a meshed support where graphene above the open structures would be freestanding.[59] The green dot (**O**) in **Figure 1** with $\omega_G{}^0$ and $\omega_{2D}{}^0$ of 1581.6 ± 0.2 and 2676.9 ± 0.7 cm^{-1}, respectively, was obtained from a freestanding graphene suspended over an open well and was considered as free of strain and nearly charge neutral. This model defines two unit vectors, $\boldsymbol{e}_T$ for strain and $\boldsymbol{e}_H$ for hole doping, and divides (ω_G, ω_{2D}) into the four quadrants (*Q*1–*Q*4). *Q*4 and *Q*1 are tensile and compressive strain, respectively, along with hole doping. Shift of (ω_G, ω_{2D}) from **O** along $\boldsymbol{e}_T$ suggests an increase in either tensile strain ($+\boldsymbol{e}_T$) or compressive strain ($-\boldsymbol{e}_T$). Any point **P** can be drawn as the **OP** vector, which can be broken down into $\boldsymbol{e}_T$, and $\boldsymbol{e}_H$ ($\mathbf{OP} = a\boldsymbol{e}_T + b\boldsymbol{e}_H$, where a and b are constants representing the magnitude of strain and hole doping, respectively).

When graphene is under compressive strain, both ω_G and ω_{2D} increase, resulting in upward shifts along the black dash line. Under tensile strain, both ω_G and ω_{2D} decrease, resulting in downward shifts along the black dash line. Results from this study showed that ω_G could shift by ≈23.5 cm^{-1} per 1% uniaxial tensile or compressive strain, while ω_{2D} could shift by ≈51.6 cm^{-1} per 1% uniaxial tensile or compressive strain.[59] This method has been used to study strain and doping in graphene due to its simplicity and the wide use of Raman spectroscopy for graphene characterization. Further vector decomposition into strain, *p*-type, and *n*-type doping, however, is challenging unless at least one component is unambiguously known. Since the analysis is referenced to a freestanding graphene and the preparation method is known to affect the degree of strain and charge doping, it is recommended that freestanding graphene sample be prepared under the conditions to be studied to obtained ($\omega_G{}^o$, $\omega_{2D}{}^o$) of the reference point O.

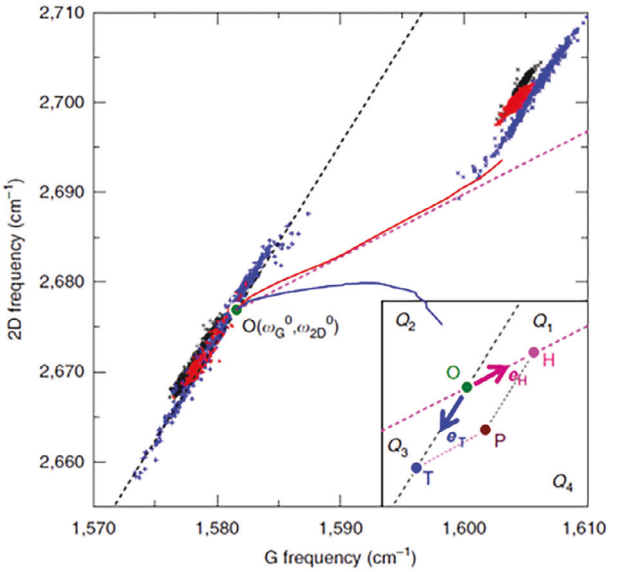

Figure 1. Raman-based vector model to determine strain and doping in graphene. The green dot (O) represents the strain- and charge-free condition from a freestanding graphene suspended over an open well. Data points are experimental values from three graphene samples shown in red, blue, and black before (+) and after (×) annealing at 400 °C. The red solid line is graphene doped with different density of holes and blue solid line is graphene doped with different density of electrons. The magenta dashed line is the experimental average (ω_G,ω_{2D}) for strain-free graphene with different hole densities. The black dashed line is the predicted trend for charge-neutral graphene under random uniaxial stress. Inset: vector model illustrating separation of strain and hole doping, with data points broken down into components along unit vectors for hole doping (e_H) and tensile strain (e_T). As hole doping or strain increases, (ω_G, ω_{2D}) will move from O along e_H or e_T. Annealing at 400 °C resulted in large increases in both ω_G and ω_{2D}, in parallel with e_T, indicating strong hole doping. Q2 and Q3 are not valid options as both electron and hole doping increase the G band frequency. Reproduced with permission.[59] Copyright 2012, American Chemical Society.

2.3. Impact of Strain on Graphene Reactivity

Several methods have been employed to create strains by substrate engineering and to study their effects on the reactivity of graphene: i) by placing graphene on nanoparticle-decorated substrates, ii) by using metal substrates having different lattice structures, and iii) by stretching or compressing a polymer substrate. Below, we discuss literature examples using each method, the effect on the reactivity of graphene, and product characterization (**Table 1**).

Table 1. Substrate-induced strain and effect on graphene reactivity.

Method for strain creation	Substrate preparation	Reaction/Reagent/Conditions	Effect on graphene reactivity	Refs.
Nanoparticles (NPs)	50 nm SiO_2 NPs deposited on silicon wafer	Aryl radical addition/4-NBD/10 mg mL^{-1} in acetonitrile, 60 min	Higher reactivity of wrinkled than flat graphene; No obvious D band in planar region; Significant increase in I_D at wrinkled regions.	[74]
	6 nm SiO_2 NPs spin coated on silicon wafer	Aryl radical addition/4-NBD/11.5 mg mL^{-1} in acetonitrile, 10 min	Higher reactivity of graphene on NPs (2.7 times) than flat substrate	[75]
	Monolayer of 114–400 nm SiO_2 NPs on silicon wafer and annealed at 350 °C in H_2/Ar for 2 h	Aryl radical addition/4-NBD/20 mM aqueous solution of 4-NBD (≈10 mL) and 1 wt.% sodium dodecyl sulfate (≈2 mL), 40 °C, 1.5 h	Enhanced functionalization of graphene in regions directly above SiO_2 NPs	[76]
Metal lattice orientation	CVD graphene grown on *p*Cu	Fluorination/XeF_2 gas/2×10^4 mbar, room temperature, 60 s	G/Cu(111): Most reactive; G/Cu(100): Variations in reactivity; G/Cu(110): Least reactive	[77]
	Epitaxial graphene grown on Cu(111)	Reductive functionalization/iodobenzene /1 mmol in THF and ($[K(15\text{-crown-}5)_2]Na$), 10 min	Epitaxial G/Cu(111): I_D/I_G increased from < 0.1 to ≈2; G/*p*Cu: No obvious increase of I_D/I_G.	[78]
	Graphene grown on Cu(111), Cu(100), or *p*Cu, G/*p*Cu transferred onto silicon wafer (G/SiO_2)	Reductive functionalization/aryl halides/1 mmol in tetrahydrofuran (THF) and $[K(15\text{-crown-}5)_2]Na$, 20 °C, 5 min	G/Cu(111): Fast and uniform functionalization (I_D/I_G = 2.3); G/Cu(100): Slow and non-uniform functionalization primarily on edges and defect lines (I_D/I_G = 0.19); G/*p*Cu: Very slow and nonuniform functionalization (I_D/I_G = 0.13); G/SiO_2: Intermediate reactivity (I_D/I_G = 1.1)	[79]
Deformation of polymer	Stretching PDMS by up to 15%	Aryl radical addition/4-NBD, 4-BBD, and 4-MBD/20 mM aqueous solutions, varying reaction time	At 15% strain, I_D/I_G of stretched graphene was twice as high as unstretched for 4-NBD and 4-BBD, and ten folds for 4-MBD.	[80]
	Uniaxial or biaxial strain induced by thermoplastic polystyrene with fluoropolymer skin layer to form 1D or 2D wrinkled graphene	Fluorination/CF_4 plasma/25 sccm CF_4, 200 mTorr, 10 W, 5 s	1D wrinkles: High-curvature sites and high reactivity at low strain (ϵ_{1D} < 0.4), formation of folds and reactivity decreased at moderate strain (ϵ_{1D} ≈0.4), decreased curvature at peak features, fewer high-curvature sites, decreased reactivity at high strain (ϵ_{1D} > 0.4). 2D wrinkles: More high-curvature sites and high reactivity at low strain (ϵ_{1D} < 0.4), high density of high-curvature sites and high reactivity at moderate strain (ϵ_{1D} ≈0.4), no significant decrease in high-curvature sites, reactivity higher than low strain but lower than moderate strain at high strain (ϵ_{1D} > 0.4).	[81]

2.3.1. Strain Generated by Decorating Substrates with Nanoparticles

Nanoparticle-decorated substrates have been used to manipulate the electronic or mechanical properties of graphene.[82–87] Nanoparticles increase the roughness of the substrate, which in turn can create wrinkles in graphene. Studies have shown the density of wrinkles increased with the nanoparticle density, irrespective of the nanoparticle diameter.[84–86] Studies have also shown that high curvatures lead to increased strain, with the curvature being defined as the inverse of the particle radius.[83] For graphene placed on closely packed SiO_2 nanoparticles of diameters ranging from 20 to 200 nm, the largest tensile strain of 0.32% was obtained on 20 nm nanoparticles along with the largest shifts in the G and 2D band to lower frequencies.[83] In addition, it has been reported that annealing graphene transferred on nanoparticle-decorated substrate created compressive strain in graphene,[75,76,82] whereas tensile strain was produced without annealing.[83,86,87] After annealing, graphene conformed more closely to the nanoparticle-induced corrugations, resulting in increased roughness and formation of suspended regions between nanoparticles. Raman G and 2D peak positions shifted to higher frequencies after annealing, suggesting the introduction of compressive strain.[82]

The Ruoff group reported the first example of using silica (SiO_2) nanoparticles to introduce strain in graphene and the effect of strain on the reaction with 4-nitrobenzenediazonium tetrafluoroborate (4-NBD, **Figure 2A**).[74] Silica nanoparticles of ≈50 nm were deposited onto silicon wafer and graphene was subsequently transferred. On a flat silicon wafer, the graphene sheet was smooth with some visible wrinkles (Figure 2B-a). The D band was absent in the smooth area (Figure 2B-d, spot 1) and very low intensity D band was seen on wrinkles or structural

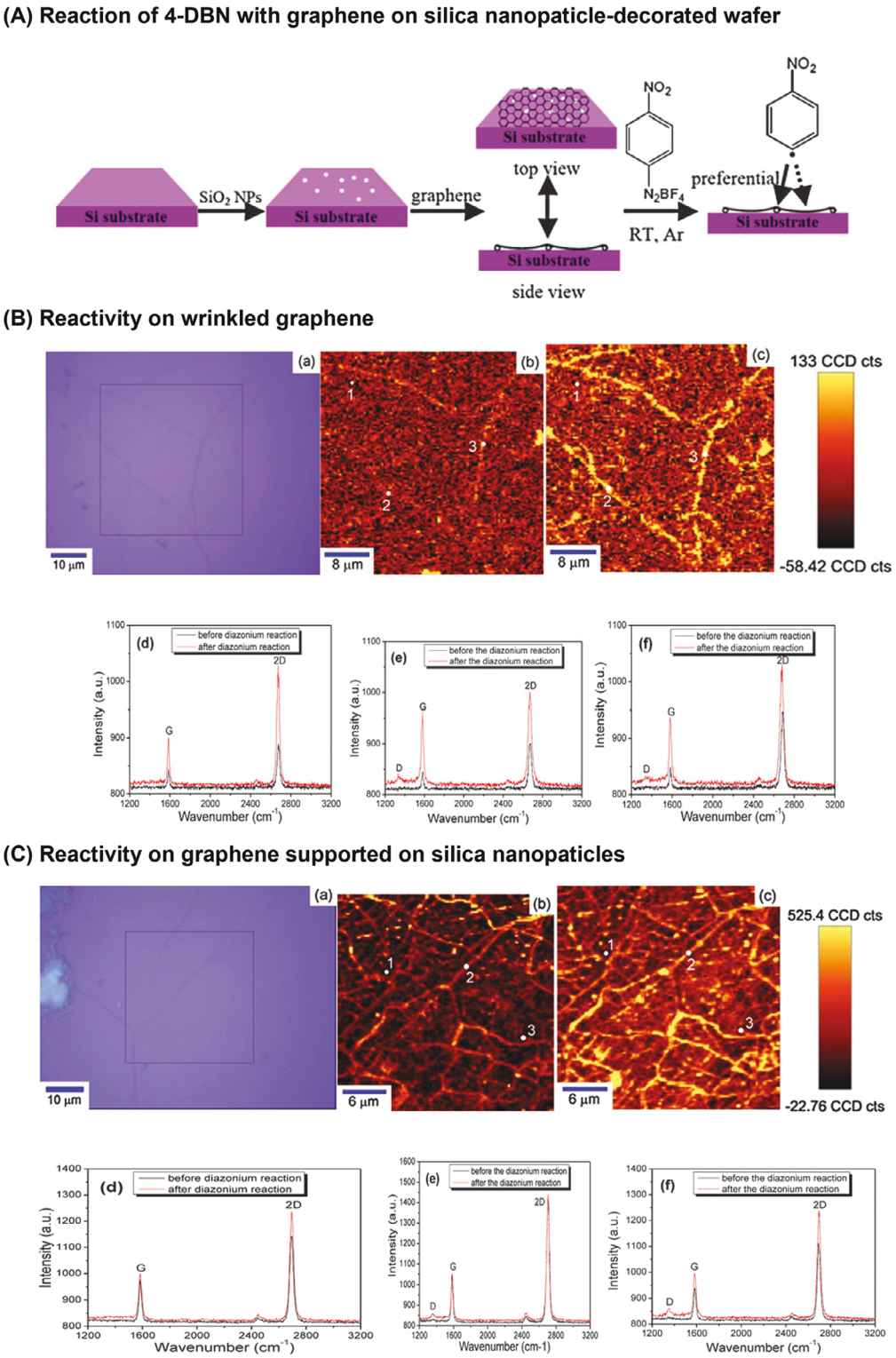

Figure 2. Graphene on silica nanoparticles-decorated substrate and reaction with 4-NBD. A) Fabrication of silica nanoparticle-decorated substrate and subsequent reaction with 4-NBD via aryl radicals. B-a) Optical image of graphene on silicon wafer. Raman maps of graphene on silicon wafer B-b) before and B-c) after reaction with 4-NBD, showing increased D band intensity at wrinkled regions. Raman spectra of graphene before and after reaction, corresponding to B-d) spot 1, (B-e) spot 2, and B-f) spot 3 as marked in (b) and (c). C-a) Optical image of graphene on silica nanoparticle-decorated wafer. Raman maps of graphene on silica nanoparticle-decorated wafer C-b) before and C-c) after reaction with 4-NBD, showing increased D band intensity at wrinkled regions and nanoparticle sites. C-d–f) Raman spectra of graphene before and after reaction, corresponding to C-d) spot 1, C-e) spot 2, and C-f) spot 3 as marked in (b) and (c). Reproduced with permission.[74] Copyright 2013, Royal Society of Chemistry.

irregularities on graphene (Figure 2B-e,f, spots 2 and 3). After reaction with 4-NBD (10 mg mL^{-1} in acetonitrile) for 60 min, there was a noticeable increase in I_D, particularly in regions corresponding to the wrinkles and high curvature areas. The I_D/I_G was ≈0.86 and ≈0.88 for spots 2 and 3, respectively (Figure 2B-e,f). No obvious D band was detected on spot 1 (Figure 2B-d), indicating low relativity of graphene on the flat wafer. Raman mapping of the D band in 1300–1400 cm^{-1} showed high I_D matching those wrinkled regions (Figure 2B-e,f), supporting that wrinkles increased the reactivity of graphene.

For graphene transferred onto silica nanoparticles, the D band intensity was still low (Figure 2C-d). Some localized regions showed slightly higher I_D, corresponding to the natural wrinkles and areas of high local curvature caused by the nanoparticles. Raman spectra taken in the flat (spot 1) and wrinkled regions (spots 2 and 3) again showed significant increase in I_D after reaction with 4-NBD with I_D/I_G of ≈0.85 and ≈0.86 for spots 2 and 3, respectively (Figure 2C-e,f). The Raman map of the D band showed high I_D matching the wrinkled regions and the areas having nanoparticles underneath. The authors attributed the enhanced reactivity to increased strain energy and reduced electronic delocalization caused by the curvature. Using the π-orbital axis vector theory, the authors demonstrated that carbon atoms in highly curved surfaces have higher chemical potential, making them more reactive than those in the flat surface. DFT calculations supported this, showing increased binding energy of nitrophenyl groups to graphene having higher surface curvature.

The Batteas group further investigated the reactivity of graphene on silica nanoparticle-decorated silicon wafer.[75] In this case, 6 nm silica nanoparticles were used and were spin-coated on the wafer. On the flat silicon wafer, the graphene surface imaged by atomic force microscopy (AFM) appeared relatively smooth with ≈12% of the surface containing wrinkles, folds, and blisters, which were attributed to incomplete adhesion of graphene to the substrate (**Figure 3**A-a,b). Graphene on silica nanoparticles appeared to be more conformed to the topography of nanoparticles underneath (Figure 3A-c,d) without the sharp features of wrinkles, folds, and blisters observed in graphene on the flat silicon wafer. The RMS roughness of graphene on silica nanoparticles, 1.10 ± 0.02 nm, was slightly higher than graphene on flat silicon wafer at 0.9 ± 0.1 nm. After reaction with 4-NBD (11.5 mg mL^{-1} in acetonitrile, under nitrogen) for 10 min, Raman maps of the D peak (1310–1410 cm^{-1}) showed an increase in I_D, particularly in regions with high curvature (Figure 3B-a,b). This result is consistent with the work of Ruoff that wrinkled graphene was more reactive toward 4-NBD than the flat graphene. For graphene on nanoparticles, the increase in I_D after reaction was much more pronounced than graphene on the flat wafer, as shown in both Raman mapping (Figure 3B-b) and Raman spectra where both the D peak and -NO_2 peak of graphene on the 6 nm nanoparticles increased after reaction with 4-NBD (blue vs red curve, Figure 3C). These results suggest that graphene supported on silica nanoparticles was not only more reactive than graphene on the flat silicon wafer, but also that the effect of nanoparticles on enhancing the reactivity of graphene was higher than natural wrinkles and folds on graphene.

Graphene on both flat and nanoparticle substrates was under compressive strain, as indicated by the negative strain values, with graphene on 6 nm silica nanoparticle films experiencing 0.10–0.20% strain (Figure 3D). The increases in the D peak and -NO_2 peak intensity were higher for graphene on 6 nm nanoparticles than the flat substrate, indicating that the strain introduced by the nanoparticles enhanced the chemical reactivity and defect formation in the graphene. Computation results showed that the activation barrier decreased with decreasing nanoparticle diameter, with smaller nanoparticles giving lower activation barrier thus higher reactivity with 4-NBD than larger nanoparticles (Figure 3E).

The Liu group fabricated close-packed silica nanoparticle (114–400 nm) monolayer on silicon wafer using the Langmuir–Blodgett technique (**Figure 4**A).[76] Graphene was transferred onto the silica nanoparticle monolayer and was then thermally annealed at 350 °C for 2 h in forming gas (H_2/Ar). The annealed graphene sheet maintained its integrity on top of the silica nanoparticle monolayer (Figure 4B-a). The thermal annealing step introduced noticeable compressive strain in graphene. After annealing, both G and 2D bands split into two peaks: one belonging to the pristine graphene and the other shifted to higher frequency and was also broad. For the 2D band, a broad peak appeared at 2715 cm^{-1}, showing a upshift of 26 cm^{-1} compared to the pristine graphene at 2689 cm^{-1}. The appearance of upshifted G and 2D bands are indicative of graphene under compressive strain (*cf.* Figure 1). The author attributed the compressive strain to the difference in thermal expansion coefficients of graphene and the silica nanoparticles. The reaction was carried out by immersing annealed graphene in 20 mM 4-DBN (10 mL) and 1 wt.% sodium dodecylsulfate aqueous solution (2 mL) at 40 °C for 1.5 h. Raman spectra showed a prominent D peak at 1350 cm^{-1} and a defect-induced D' peak at 1620 cm^{-1} after the reaction (Figure 4D). The authors employed scanning electron microscopy (SEM) and AFM to conclude site-selective functionalization of graphene in areas in contact with underneath nanoparticles. Both SEM (Figure 4B-c) and AFM (Figure 4B-d) showed periodic spheres with a periodicity (145–170 nm) matching that of the original close-packed nanoparticles (≈150 nm, Figure 4B-a). On the other hand, uniform surface was observed without reaction (top insert, Figure 4B-c) or reaction with graphene on a flat wafer (bottom insert, Figure 4B-c). Computations revealed that both tensile and compressive strains decreased the reaction energy, with compressive strain having a greater effect on enhancing the reactivity of graphene, especially when strain exceeded 0.02% (Figure 4E).

2.3.2. Strain Generated by Crystal Lattice Orientation of Metal Substrate

Graphene grown on Cu foils by CVD possesses strain due to lattice orientation of the Cu substrate.[88–90] Kolbac et al. reported that graphene on Cu(111) exhibited uniform biaxial compressive strain (≈0.3%) and *n*-type doping with a Fermi level shift of ≈250 meV, whereas graphene on Cu(100) and Cu(110) had lower strain and doping levels.[88,89] When CVD graphene is cooled, the higher contraction of Cu than graphene generates compressive constraint in graphene. Additionally, higher compressive strain

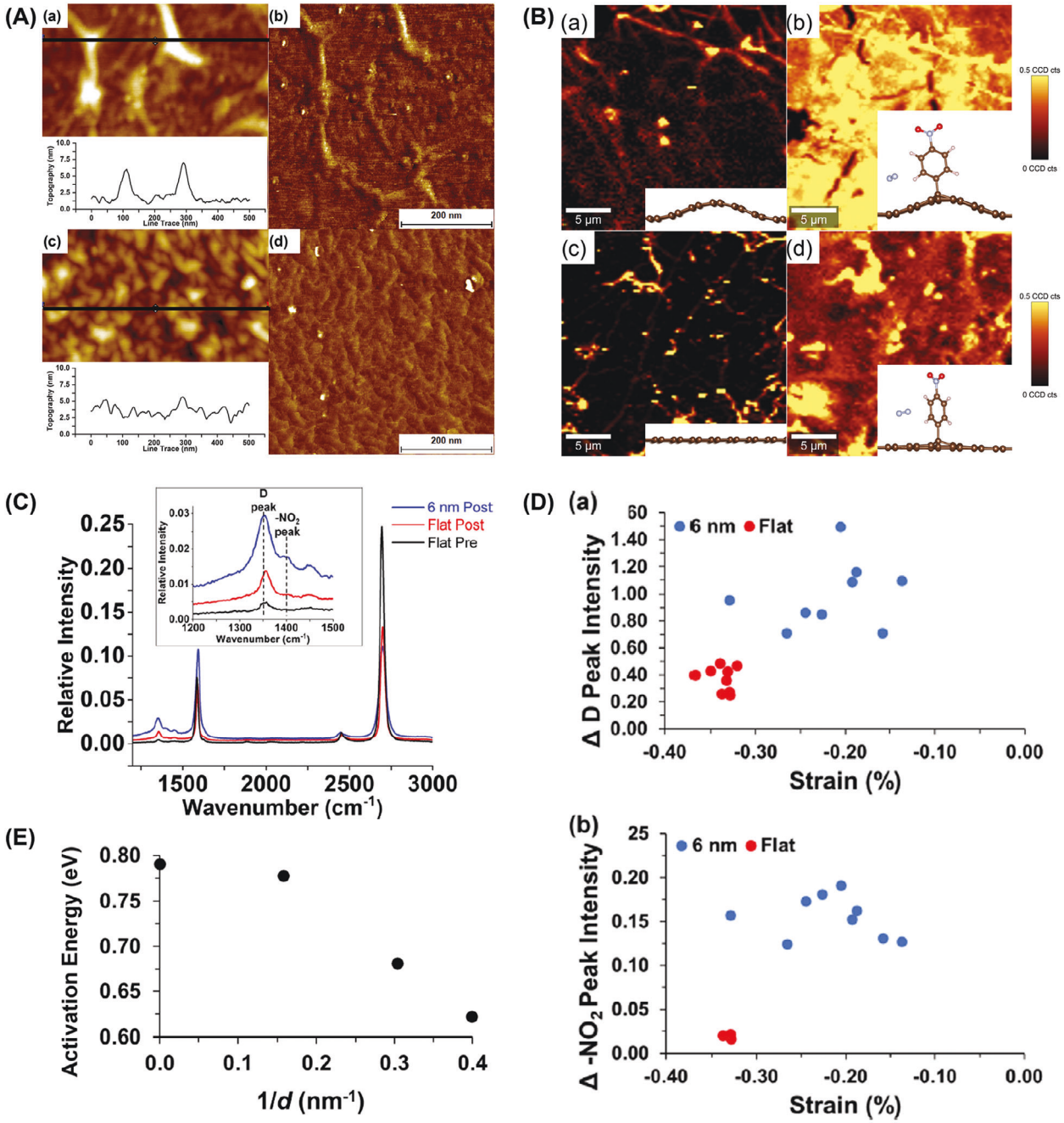

Figure 3. Graphene on spin-coated 6 nm silica nanoparticles and reaction with 4-NBD. A) AFM topography and cross section height profile of graphene on A-a,b) flat silicon wafer, A-c,d) spin-coated 6 nm silica nanoparticle film. B) Raman maps of the graphene D peak normalized to the Si peak on B-a,b) spin-coated 6 nm silica nanoparticle film, B-c,d) flat silicon wafer before (left images) and after (right images) reaction with 4-NBD. C) Raman spectra showing the D and -NO_2 peak positions for graphene on 6 nm silica nanoparticle film and flat silicon wafer before and after reaction with 4-NBD. D) Increase in D-a) I_D/I_{Si}, D-b) I_{NO2}/I_{Si} versus initial average uniaxial strain for graphene on 6 nm silica nanoparticle film and flat silicon wafer. E) Activation barrier for the reaction with 4-NBD as a function of the nanoparticle diameter calculated using the climbing image nudged elastic band method. For the flat silicon wafer, 1/d = 0. Reproduced with permission.[75] Copyright 2022, American Chemical Society.

(0.25–0.40%) was found in regions where graphene is epitaxial with the underlying Cu than regions that are not epitaxial (0.20–0.25%).[78] The epitaxial graphene grown on single crystal Cu(111) can be furthermore wrinkle free. Density functional theory (DFT) calculations suggest a large frictional force between the epitaxial graphene and the Cu(111) substrate, and this becomes an energy barrier preventing the formation of wrinkles in the graphene.[78]

Kalbac et al. carried out fluorination reaction using xenon difluoride (XeF_2) on graphene grown on polycrystalline Cu (*p*Cu)

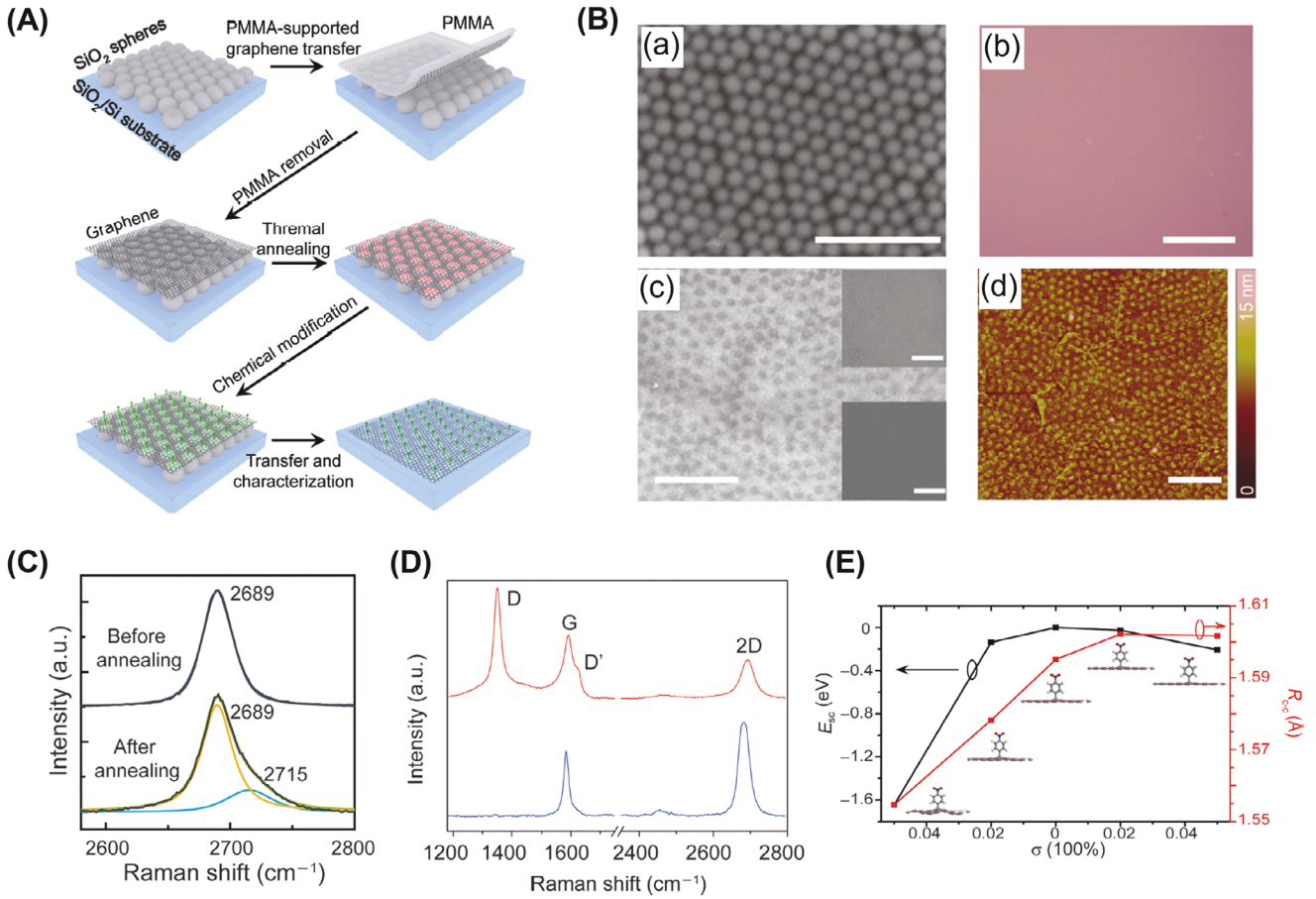

Figure 4. Graphene on periodically patterned silica nanoparticles and reaction with 4-NBD. A) Schematic of the experimental protocol. B-a) SEM image of graphene on periodically patterned 150 nm silica nanoparticles after annealing. Scale bar: 1 µm. B-b) Optical image of 4-NBD-treated graphene after transferring to silicon wafer. Scale bar: 50 µm. B-c) SEM image of graphene after reaction with 4-NBD. Inserts are graphene on a flat wafer before (top) and after reaction (bottom). Scale bar: 1 µm. C) Raman 2D peak before and after annealing. D) Raman spectra before (blue) and after (red) reaction. E) Calculated reaction energy difference of graphene with and without strain energy (E_{sc}) or bond length ($R_{C\text{-}C}$) versus strain. Reproduced with permission.[76] Copyright 2016, Wiley-VCH.

foil and studied the fluorination reactivity in regions of *p*Cu with different crystal orientations.[77] The *p*Cu foil contains different grains with grain boundaries clearly visible (**Figure** 5A). The fluorination reaction involves breaking carbon–carbon double bonds in graphene to form C—F bonds, generating sp^3 carbons and therefore D peak in the product. Figure 5B are plots of Raman I_D/I_G and I_{2D}/I_G of fluorinated graphene versus copper grain orientation. The results varied across different grain orientations, with the highest fluorination observed for graphene on Cu(111), while graphene on grains close to Cu(110) was the least reactive. The authors attributed this reactivity trend to strain. Graphene was uniformly compressed with 0.3% biaxial strain on Cu(111), 0.05–0.3% on Cu(110), and 0.1% on Cu(100). While the highest reactivity on Cu(111) was consistent with the largest strain on Cu(111), for graphene on Cu(100), which was supposed to yield the lowest reactivity according to the strain level, some areas (e.g., 1 and 5) showed high fluorination similar to that of graphene on Cu(111).

Ruoff and coworkers grew CVD graphene on single crystal Cu(111) and on *p*Cu, and compared the extent of functionalization of graphene in the reactions with iodobenzene and iodoaniline.[78] The epitaxial graphene grown on Cu(111) was wrinkle free, compared to wrinkled graphene grown on *p*Cu. The authors attributed this to the two orders of magnitude higher friction forces between epitaxial graphene and Cu(111) than between non-epitaxial graphene and *p*Cu, which prevents strain relaxation through the loss of adhesion to form wrinkles. Epitaxial graphene on Cu(111) showed significant compressive strain with G-band frequencies ranging from 1590 to 1610 cm^{-1} (**Figure** 6A-a), whereas non-epitaxial graphene on *p*Cu exhibited lower strain with smaller G-band frequency variation from 1582 to 1585 cm^{-1} (Figure 6A-b). The plot of ω_{2D} versus ω_G gave a slope of 2.8, $\Delta\omega_G/\Delta\epsilon = -56$ cm^{-1}/%, and $\Delta\omega_{2D}/\Delta\epsilon = -155$ cm^{-1}/% (Figure 6A-c). These are indicative of compressive strain without doping (*cf.* Figure 1). The absence of G peak splitting supported biaxial strain.[67,69]

The ability to prepare wrinkle-free epitaxial graphene enabled the study of compressive strain on the reactivity of graphene without the contribution of wrinkles. The reaction tested was reduction with [K(15-crown-5)$_2$]Na followed by the addition of iodobenzene to give phenyl-functionalized graphene.[91] After the reaction, I_D/I_G of epitaxial graphene on Cu(111) increased from

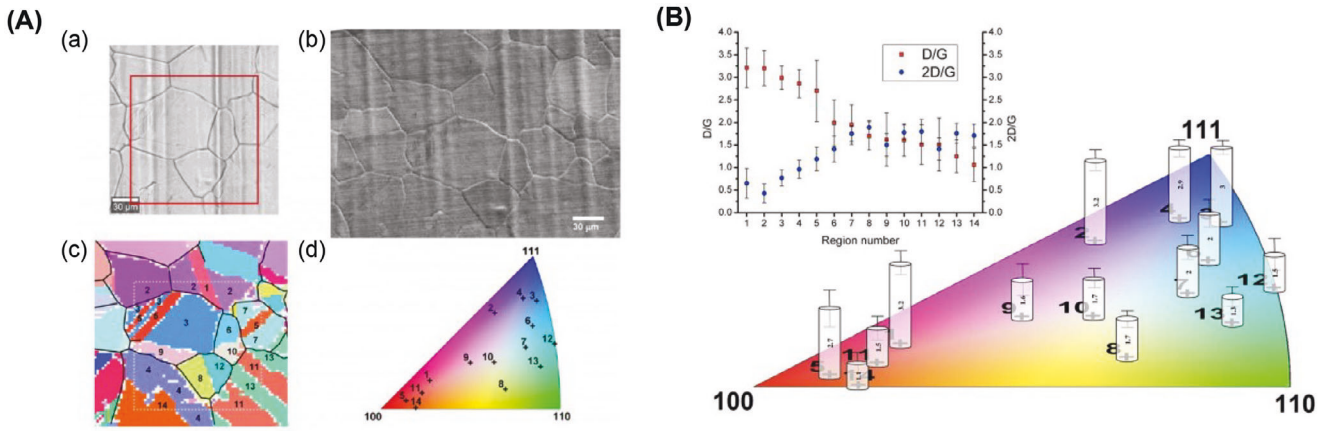

Figure 5. Effect of copper crystal orientation on the fluorination of graphene. A-a) Optical and A-b) SEM images of *p*Cu foil showing various grains and grain boundaries. A-c) Electron backscatter diffraction (EBSD) map of *p*Cu foil. Colors represent different orientations. A-d) Inverse pole figure legend correlates colors to crystalline orientations. B) Raman I_D/I_G and I_{2D}/I_G of fluorinated graphene versus copper grain orientation. The region numbers are the same as those in the EBSD map and IPF diagram. Reproduced with permission.[77] Copyright 2017, Wiley-VCH.

< 0.1 to up to 2 (Figure 6B-a–c), whereas no significant change in I_D/I_G was seen for graphene on *p*Cu except in the edge areas (Figure 6B-d–f). The authors concluded that the non-epitaxial graphene was not reactive toward iodobenzene even on wrinkled areas. Reaction with iodoaniline gave similar results in Raman characteristics. The authors attributed the higher reactivity of epitaxial graphene on Cu(111) to a lower product formation energy and/or a lower activation energy as a result of the high compressive strain in epitaxial graphene.

Using the same reductive functionalization reaction, Ruoff and coworkers further investigated the reactivity of graphene supported on Cu(111), Cu(100), and *p*Cu (**Figure** 7A-a).[79] While the D peak was absent in the initial graphene (Figure 7A-b), after reaction with iodobenzene, a significantly higher D peak intensity was observed for graphene on Cu(111) (I_D/I_G = 2.3) compared to Cu(100) (I_D/I_G = 0.19), *p*-Cu (I_D/I_G = 0.13), and SiO_2 (I_D/I_G = 1.1) (Figure 7A-c). Bromobenzene showed the same trend, although the overall degree of functionalization was lower than iodobenzene (Figure 7A-d). Graphene on Cu(111) exhibited shifts of ω_G and ω_{2D} to higher freqencies across the entire graphene with $\Delta\omega_{2D}/\Delta\omega_G$ of 2.47 ± 0.54 and a compressive strain of −0.29 ± 0.08% calculated from$\partial\omega_G/\partial\epsilon$, while the strain of graphene on Cu(100) and *p*-Cu were lower at −0.09% and −0.05%, respectively (Figure 7B). Computations on relative energies of the reactants, transition states, and products revealed that increasing compressive strain in graphene lowered the energy barrier of the reaction as well as the energy of the product (Figure 7C).

2.3.3. Strain Generated by Deformation of Polymer Substrate

When force is applied to a polymer substrate, it can undergo significant deformation, particularly in elastomers such as

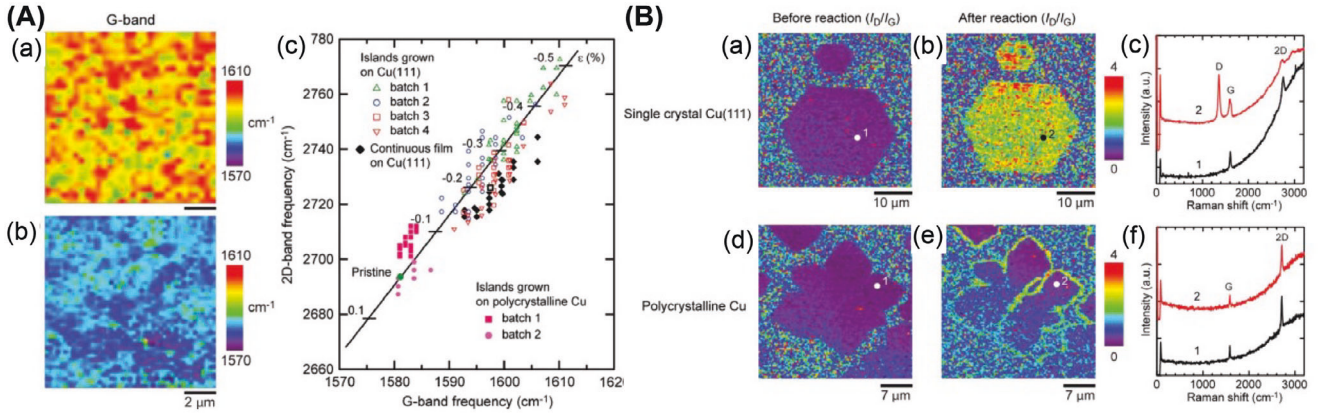

Figure 6. Graphene on copper and reaction with iodobenzene. A) Raman maps of G-band frequency for A-a) epitaxial graphene on Cu(111) and A-b) non-epitaxial graphene on *p*Cu. A-c) Correlation between G- and 2D-band frequencies. The green dot is the reference point of unstrained and undoped graphene (ω_{2D}: 2692 cm^{-1} and ω_G: 1582 cm^{-1}). The fitted line shows the biaxial strain in epitaxial graphene. ϵ is strain. B) Raman maps of I_D/I_G and spectra before and after reaction with iodobenzene for B-a–c) epitaxial graphene on Cu(111) and B-d–f) non-epitaxial graphene on *p*Cu. Reproduced with permission.[78] Copyright 2018, Wiley-VCH.

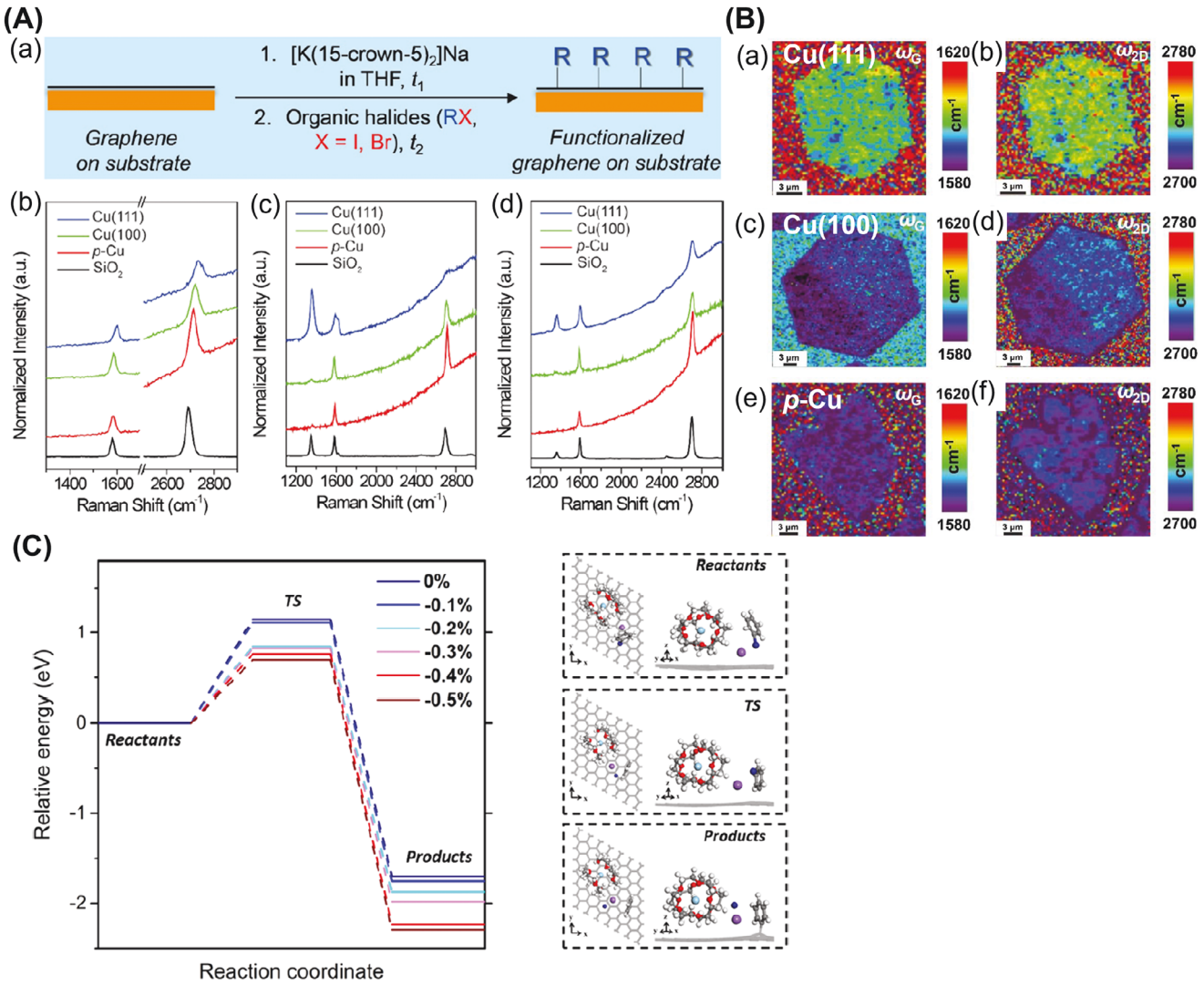

Figure 7. Graphene on Cu(111), Cu(100), *p*-Cu and reaction with iodobenzene. A-a) Reaction and conditions: $[[K(15\text{-crown-}5)_2]Na]_0$ ($[C_{NaK}]_0$) = 0.02 M; t_1 = 5 min; t_2 = 5 min; temperature = 20 °C. Raman spectra A-b) before and after reaction with A-c) iodobenzene or A-d) bromobenzene. B) SEM images of graphene islands on B-a,b) Cu(111), B-c,d) Cu(100), and B-e,f) *p*-Cu. C) Raman ω_G and ω_{2D} frequency maps of monolayer graphene islands on different copper substrates. D) Computed activation and product energies at different compression strains. Reproduced with permission from.[79] Copyright 2019, American Chemical Society.

polydimethylsiloxane (PDMS). This deformation can transfer strain directly to the supported graphene sheet or induce wrinkles in graphene when the polymer relaxes. Polymers generally maintain good contact with graphene. After the mechanical force is removed, the relaxation of the polymer substrate can induce strains in graphene as it conforms to the underlying polymer layer.[81,92,93] It has been reported that this kind of mechanical deformation does not cause defects in graphene and the strain is uniformly distributed unless excessively large strains are applied.[80,94–97] A drawback of this approach is that the transfer of strain from the polymer substrate to graphene may not be complete owing to the loss of strain caused by insufficient interfacial adhesion between graphene and the polymer.[95,97] It is thus difficult to measure the "real" strain on graphene.[80] For elastomers such as PDMS, stretching it not only elongates graphene but also compresses it in the perpendicular direction.

Ago and coworkers used PDMS as the substrate and studied the reaction of stretched graphene with aryl diazonium salts, including 4-NBD, 4-bromobenzenediazonium (4-BBD) and 4-methoxybenzenediazonium (4-MBD).[80] The stretching was done on a custom-built apparatus where PDMS was fixed and stretched by applying a constant strain (**Figure 8**A). Results showed that by applying strains, both the rate of reaction and the degree of functionalization on graphene increased for all three diazonium salts tested. The higher the applied strain, the faster the reaction and the higher the degree of functionalization, with the highest strain applied at 15% consistently giving the highest I_D/I_G. The authors hypothesized that the external stress affected the orbital hybridization and made the p_z electrons in graphene

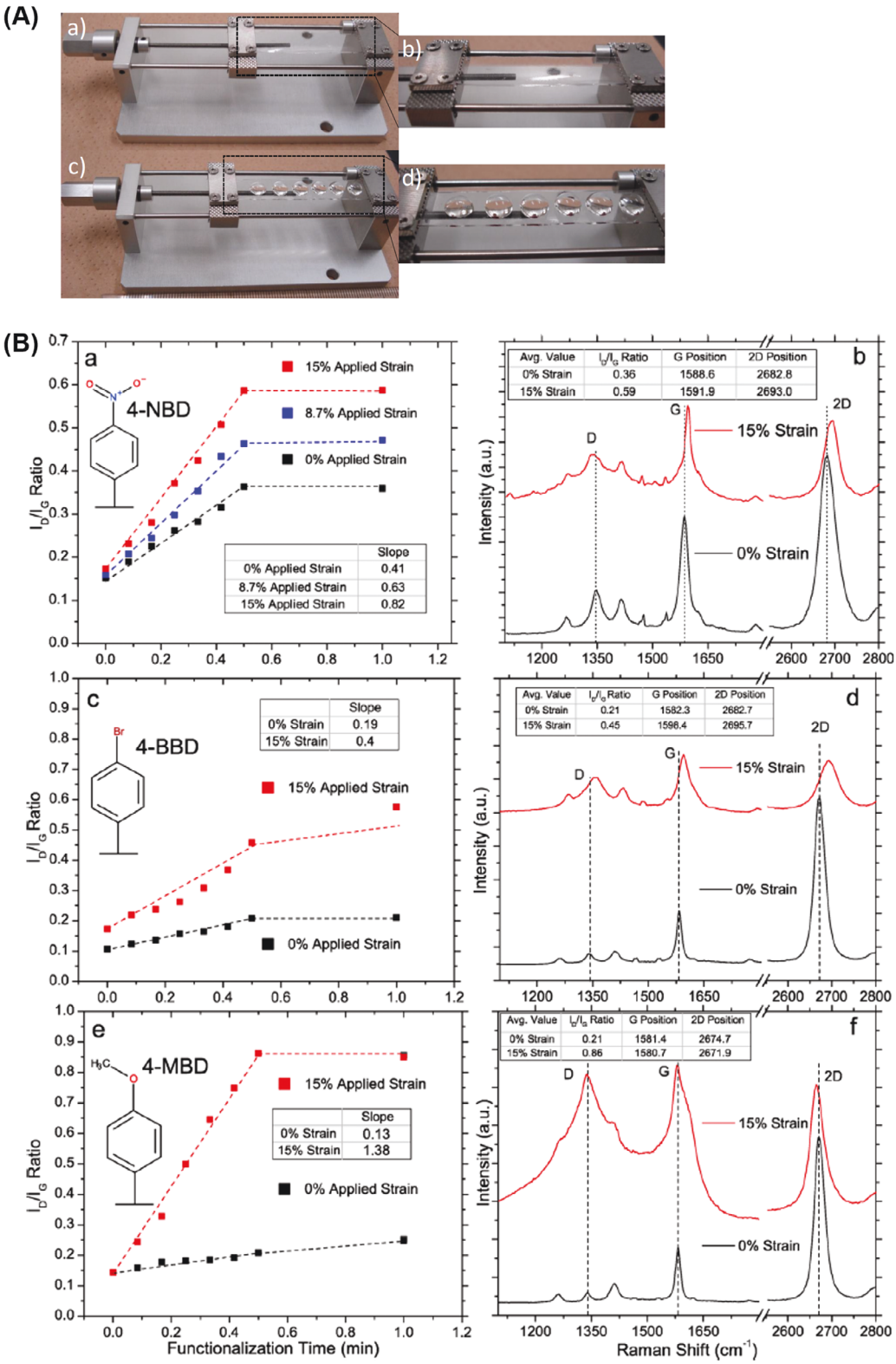

Figure 8. Graphene on stretched PDMS and reaction with diazonium salts. A-a,b) Experimental setup for stretching PDMS. Samples were prepared by transferring CVD graphene from Cu to PDMS. A-c,d) Droplets of 20 mM aqueous solution of the diazonium salt on graphene. B) I_D/I_G versus reaction time for unstrained and strained graphene (left panels) and Raman spectra at 30 s reaction time (right panels) for B-a,b) 4-NBD, B-c,d) 4-BBD, and B-e,f) 4-MBD. Strain = $(L_f - L_o) / L_o \times 100\%$, where L_f is the final length and L_o is the original length of PDMS. Reproduced with permission.[80] Copyright 2013, American Chemical Society.

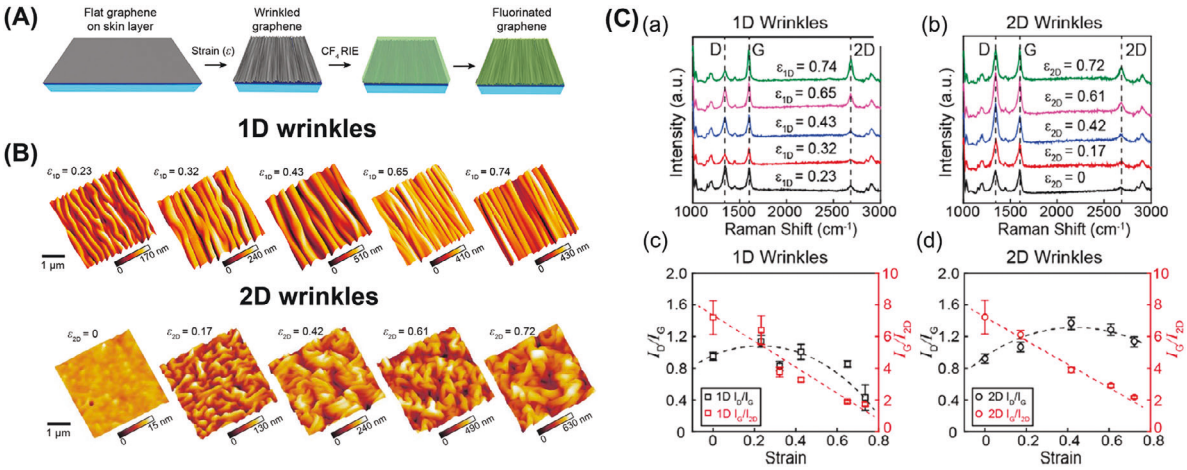

Figure 9. Graphene on stretched polymer layer in fluorination reaction. A) Fabrication of graphene on stretched polymer layer and subsequent fluorination reaction. B) AFM images of 1D and 2D wrinkles formed by relieving different amount of strain in the substrate. C-a,b) Raman spectra and C-c,d) I_D/I_G and I_G/I_{2D} of 1D and 2D wrinkled graphene at different substrate strains after fluorination. For 1D wrinkles and crumples, strain (ϵ_{1D}) was calculated by measuring the change in the length of PS substrate before and after strain relief: $\epsilon_{1D} = (L_0 - L_R) / L_0$, where L_0 is the initial length and L_R is the length after shrinking. For 2D wrinkles, strain (ϵ_{2D}) was calculated by measuring the change in the area of PS substrate before and after strain relief: $\epsilon_{2D} = (A_0 - A_R) / A_0$, where A_0 is the initial area and A_R is the area after shrinking. Reproduced with permission.[81] Copyright 2019, American Chemical Society.

more available to react with the phenyl radicals perpendicular to graphene. The authors also assumed that the electron-hole puddle effect from the substrate remained constant as PDMS is an insulator.

By stretching the polymer substrate and patterning the strain in a controlled fashion, the Odom group created multiscale wrinkles and crumples on graphene, and demonstrated spatially selective fluorination using CF_4 plasma (**Figure 9**A).[81] The authors found that uni-directional stretching produced aligned 1D wrinkles and biaxial stretching produced randomly oriented 2D wrinkles (Figure 9B). The wavelength of wrinkles can be controlled by adjusting the thickness of the soft skin layer. For both 1D and 2D wrinkles, higher curvature sites were seen at moderate strains and decreased at higher strains (Figure 9B). Overall, 2D wrinkles had more high-curvature sites than 1D wrinkles at similar applied strains. After fluorination, I_D/I_G initially increased with strain, but decreased at higher strains for both 1D and 2D wrinkles (Figure 9C), which was consistent with lower number of high-curvature sites at higher strains. The decrease for 2D wrinkles was smaller than 1D wrinkles at similar strains, which was also consistent with more high-curvature sites in 2D wrinkles. The authors also created crumples using polystyrene without the fluoropolymer as the adhesive skin layer. The larger number of high curvature sites in crumples led to greater extent of fluorination on graphene. This study highlighted the role of high curvature wrinkles in enhancing the reactivity of graphene.

3. Effect of Charge Doping on the Reactivity of Graphene

3.1. Charge Doping in Graphene

Charge doping involves the introduction of charge carriers, either electrons or holes, in graphene. The outcome of charge doping is the modification of its electronic properties such the Fermi level, bandgap, and conductivity.[39,52,98–100] Methods for introducing charge doping include using substrates such as metals and oxides, substitutional doping where carbon atoms are replaced by heteroatoms like nitrogen or boron, doping by electron-donating or electron-withdrawing species, and by applying electric field.[52,98,101] Functionalization of substrates with alkyl groups generally screen surface charges and lower doping. The type and the doping level can affect the chemical reactivity of graphene depending on the type of reactions. The *n*-type doping has shown to increase the reactivity of graphene toward electrophilic species, while *p*-type doping increases reactivity toward nucleophilic species. However, the process of doping may be influenced by other factors, including strains, which can complicate the analysis.

3.2. Characterization of Doping in Graphene

Similar to strain, Raman spectroscopy is the most widely used technique for the characterization of charge doping in graphene (*cf.* Figure 1). Using pristine monolayer graphene prepared by micromechanical exfoliation of graphite on silicon wafer and by applying a gate voltage to control the electron or hole concentration, Ferrari and coworkers have conducted a series of experiments to study the effect of doping on the Raman bands of graphene.[102–105] The conclusions can be summarized as follows: i) The G peak shifts to higher frequencies for both electron and hole doping. ii) The 2D peak also shifts, but its behavior is primarily due to charge transfer. Hole doping shifts the 2D peak to higher frequencies. For electron doping, the 2D peak remains unchanged at up to 3.2×10^{13} cm$^-$ and shifts to lower frequencies at higher electron concentrations. iii) The full-width-at-half maximum (FWHM) of the G peak decreases for both electron and hole doping. (iv) I_{2D}/I_G decreases with increasing electron

and hole doping. It was suggested that I_{2D}/I_G should be used to monitor the doping level in graphene rather than the number of layers.

Inverse photoelectron spectroscopy (IPES) has been used to characterize charge transfer between graphene and the substrate.[106–108] IPES detects specific unoccupied electronic states in a material. For graphene supported on a substrate, the charge transfer between the substrate and graphene can be quantified by measuring the position of a specific conduction band relative to the Fermi level in the IPES spectrum. For electron doping (*n*-doping) where electrons are transferred to graphene from the substrate, the Fermi level shifts upwards toward the conduction band, whereas for hole doping (*p*-doping) where electrons are transferred from graphene to the substrate, the Fermi level shifts downwards toward the valence band. Kelber et al. collected IPES spectra of graphene on various substrates and determined the charge transfer from the substrate to graphene to be −0.07 electron/carbon for BN(0001)/Ru(0001) heterostructure, -0.06 electron/carbon for Ru(0001), -0.03 electron/carbon *p*Ni and *p*Cu, and +0.02 electron/carbon for MgO(111).[106] The Raman peak positions were in agreement with the trend discussed above, with the G band shifting to higher frequencies for graphene on all substrates, and the 2D band shifting to higher frequencies for graphene on MgO and to lower frequencies for graphene on other substrates.

Angle-resolved photoemission spectroscopy (ARPES) is another technique that can be used to characterize charge doping.[40,109] It maps the electronic band structure by measuring electron energies and emission angles from the surface of the material under photon illumination.[40] In substrate-supported graphene, ARPES can detect shifts in the Fermi level, which reveals the type of charge transfer between graphene and the substrate. For example, Dedkov et al. employed ARPES to study the modification of the valence band states of graphene on Ni and found a significantly larger binding energy of graphene π-states (≈2.4 eV) compared to pure graphite, indicating strong hybridization of graphene π states with Ni 3d states and transfer from Ni to graphene.[109]

Scanning tunneling microscopy density of states (STM DOS) measures the local density of states (DOS) near the Fermi level.[40,110,111] In STM, a sharp metallic tip scans in close proximity to a conductive sample, such as graphene, while a bias voltage is applied, causing electrons to tunnel between the tip and the sample. This tunneling current is sensitive to the DOS of the sample, allowing STM to map electronic states as a function of energy and position. In graphene, STM DOS measurements can reveal shifts in the Dirac point, which occurs when graphene is doped and shifts in energy. By quantifying this shift, STM DOS can characterize the extent and type of charge doping (electron- or hole-doping) in graphene. For lattice-mismatched systems, moiré patterns arise due to the periodic overlay of graphene with metal substrates, creating spatial variations in DOS due to differing lattice constants between graphene and the metal.[40,110] On substrates such as Ru(0001) and Ir(111), these moiré patterns can induce strong variations in the local electronic environment, leading to regions with different levels of interaction between the π orbitals of graphene and the d orbitals of the metal. By measuring the DOS with STM, spatial variations of charge doping within graphene can be determined.

3.3. Impact of Charge Doping on the Reactivity of Graphene

Literature examples employing charge doping through substrates to investigate graphene reactivity can be broadly categorized into metal substrates (**Table 2**) and non-metal substrates (**Table 3**). Below, we discuss the sources of charge doping for each substrate type and provide representative examples, emphasizing the effect of charge doping on graphene functionalization.

3.3.1. Metal Substrate-Induced Charge Doping and Impact on Graphene Reactivity

The binding energy of metals with graphene varies widely depending on the metal and affects graphene properties including charge doping.[39–41] Strongly interacting metals, such as Co (0001), Ni (111), Ru (0001), and Rh (111), exhibit binding energies ≈−1 to −1.7 eV and typically form closer (e.g., graphene-metal distance of 2.1–2.2 Å), more stable interfaces with graphene. This strong interaction often involves hybridization between graphene π orbitals and metal d orbitals and can alter the electronic structure of graphene, sometimes disrupting its Dirac cone. In contrast, metals like Cu (111), Pt (111), and Au (111) have weaker binding interactions and show larger separation distances from graphene (3–4 Å) and lower binding energies (> −2 eV) with minimal orbital hybridization.

In many cases, strong interacting metals led to increased reactivity of graphene. For instance, Ni as the substrate has shown enhanced reactivity of graphene toward CO chemisorption,[28,112,122,123] nitrene cycloaddition,[113] and Diels-Alder reaction.[114] Ru(0001) as the substrate has shown enhanced reactivity of graphene toward covalent functionalization with cyanomethyl radicals[118] and carbene.[115] The graphene-metal binding can also be modified, for example, through the intercalation of reactive species such as oxygen.[124] Before oxygen intercalation, graphene on Ru(0001) exhibited strong hybridization with the *d* orbital in Ru, resulting in a downward shift of the π band and a gap between π and π^* states near the Fermi energy.[124] Post intercalation, the π-*d* hybridization was lifted, and well-defined graphene π bands with linear dispersion reappeared, indicating minimal interactions with the underlying metal.

The graphene-metal systems have been classified into two broad categories: lattice-matched and lattice-mismatched.[39,40] For lattice-matched systems, the lattice constants of the metal and graphene are similar, resulting in a commensurate interface such as in the cases of Ni(111) and Co(0001). For lattice-mismatched systems, the lattice constants of the metal and graphene differ, leading to an incommensurate interface such as in the cases of Ir(111), Ru(0001), and Pt(111). Moiré patterns arise in graphene on lattice-mismatched metal substrates.[40] Graphene has a honeycomb lattice structure with a specific periodicity, while metal surfaces have different lattice structures and periodicities. When graphene is placed on such a metal substrate, the slight misalignment or difference in atomic spacing causes periodic overlaps and shifts between the two lattices as they try to align. This results in a larger-scale interference pattern known as the moiré pattern, where distinct repeating regions form across the surface. These moiré patterns create spatially varying regions of electronic

Table 2. Metal substrates-induced charge doping and effect on graphene reactivity.

Substrate	Reaction/Reagents/Conditions	Effect on graphene reactivity	Refs.
Graphene grown on Ni(111)	Chemisorption/0.5-40 L CO/87 K	Enhanced chemisorption of CO on G/Ni(111)	[112]
Graphene transferred onto *p*Ni, *p*Cu, silicon wafer	Cycloaddition/PFPA/NMP, irradiation (> 280 nm)	Reactivity: G/*p*Ni (I_D/I_G: 0.1-0.53) > G/*p*Cu (I_D/I_G: 0.12-0.4) > G/SiO_2 (I_D/I_G: 0.05-0.2)	[113]
Graphene transferred onto *p*Ni, *p*Ni, silicon wafer	Diels-Alder reaction/DMBD, MAH/*p*-xylene, 50, 100, or 150 °C.	Rate constants for G/Ni: 1.8–2.2 times higher than G/SiO_2 for DMBD, 1.8–2.4 times higher than G/SiO_2 for MAH.	[114]
Graphene grown on Pt(111), Ru(0001), or Ru(0001) with O_2 intercalation	NHC/$(iPr)_2BIMCF_3{\cdot}H_2CO_3$/UHV, 350–400 K.	NHC adsorbed stronger on *p*-doped G/Pt(111) than *n*-doped G/Ru(0001); O_2 intercalation increased *p*-doping and NHC adsorption.	[115]
Graphene grown on Ir(111)	Hydrogenation/2100 K hot H-atom beam, $\approx 10^{13}$–10^{14} atoms/cm^2•s, room temperature	Preferential adsorption of H atoms at specific moiré superlattice of graphene on Ir(111), forming graphane-like islands.	[116]
Graphene grown on Ir(111)	Cycloaddition/iron-phthalocyanines/cryogenic temperature	Cycloaddition with FePc occurred on localized dangling bonds in top-fcc moiré registry of graphene on Ir(111)	[117]
Graphene grown on Ru(0001) or Ir(111)	Radical reaction/$\approx 1 \times 10^{-6}$ Torr acetonitrile/UHV, 80 K	G/Ru(0001): Strong binding of cyanomethyl radicals on HCP-Top sites; G/Ir(111): No reaction	[118]
Graphene grown on Cu(111) or Cu(115)	Electrochemistry/4-iodoaniline/$TBAPF_6$ in acetonitrile	Higher reactivity of G/Cu(115) than G/Cu(111)	[119]
Graphene transferred to silicon wafer or annealed *p*Cu (Cu_{Trans}) and graphene grown on *p*Cu (Cu_{CVD})	UVO oxidation/O_2 in closed UV-Ozone chamber/30 min	G/SiO_2: High oxidation with disappearance of 2D peak; G/Cu_{Trans}: Very low oxidation; G/Cu_{CVD}: Minimum/No oxidation	[120]
Graphene grown on *p*Cu, silicon wafer, or copper-coated silicon (Cu/Si); Graphene (2-3 layers) grown on *p*Ni (FLG/*p*Ni)	Thermal oxidation/Argon with trace amount of O_2 (<3 ppm)/600 °C, 2 h	G/*p*Cu: Significant decreases in I_D and I_G and severe oxidative degradation of graphene; G/SiO_2: Slight decreases in I_D and I_G; G/Cu/Si: Complete disappearance of G and 2D peaks; FLG/*p*Ni: Mostly intact G and 2D peaks.	[121]

interaction between graphene and the metal. In certain areas of the pattern, the graphene atoms are closer to the metal surface, leading to stronger interactions, while in other areas, the separation is larger, resulting in weaker interactions. The unique periodicities in the moiré pattern have been employed to create spatially functionalized graphene surfaces.[116–118]

The Vattuone group studied the chemisorption of CO on graphene grown on Ni(111).[112] High-resolution electron energy loss spectroscopy (HREELS) was employed to measure the vibrational modes of CO adsorbed on graphene/Ni(111) under different conditions (**Figure 10A**). After graphene/Ni(111) was exposed to CO at room temperature, no significant peaks related to CO was observed. At 87 K and 0.5 L of CO exposure, the HREELS spectrum showed significant energy losses at 259 and 48 meV, corresponding to the internal CO stretching and the CO-surface stretching, confirming the chemisorption of CO on graphene/Ni(111). With higher exposure of CO at 40 L, the intensities of the vibrational signals increased, indicating higher CO adsorption. Computation from Silvestrelli and coworkers provided theoretical support of these experimental results, showing that hybridization between graphene π orbitals and Ni *d* orbitals led to the formation of a chemisorbed ethylene dione complex (C_2O_2) on Ni(111)-supported graphene (Figure 10B), while CO only physisorbed on free-standing graphene.[122] Vattuone group also showed that for graphene defect sites created by ion bombardment, CO adsorption was significant on graphene supported on Ni(111) but not on *p*Cu.[28]

We investigated the reactivity of metal-supported graphene with nitrenes photochemically generated from perfluorophenyl azides (PFPA) (**Figure 11A**).[113] Graphene supported on Ni (G/Ni) displayed significantly diminished Raman signal intensities, consistent with the strong interaction between Ni and graphene leading to loss of phonon-photon resonance in graphene. After reaction with PFPA, G/Ni showed the most significant increase in the D band intensity, followed by graphene on Cu (G/Cu) and graphene on silicon wafer (G/SiO_2/Si) (Figure 11B-a). Analysis of I_D/I_G gave the similar trend of G/Ni > G/Cu > G/SiO_2/Si (Figure 11B-b), demonstrating substrate-dependent reactivity. Scatter plots (Figure 11B-c) revealed that 2D and G band shifts were larger for graphene on Ni and Cu than on SiO_2. I_{2D}/I_G (Figure 11B-d) was lower for graphene on Ni and Cu which was in the range of 2.5–6 compared to graphene on SiO_2 in the range of 3.5–7. The FWHMs for the G and 2D band were wider for graphene on Ni and Cu, indicating increased functionalization. The experimental results are supported by computation. DFT calculations show that the charge density differences (Δq) when a singlet nitrene is adsorbed on G/Ni is the highest at -0.56e, lower on G/Cu at -0.44e, and on G/SiO_2/Si at −0.31e (Figure 11C), indicating that the metal substrate increases the electron transfer from graphene to the singlet nitrene, with Ni

Table 3. Non-metal substrates-induced charge doping and effect on graphene reactivity.

Substrate	Reaction/Reagent/Conditions	Effect on graphene reactivity	Refs.
Plasma-cleaned silicon wafer (SiO_2), Sapphire (Al_2O_3), OTS-modified silicon wafer, hBN	Aryl radical addition/4-NBD/0.5 wt.% SDS, ≈35 °C, 16.5 h	High reactivity for G/SiO_2 (I_D/I_G = 1.4) and G/Al_2O_3 (I_D/I_G = 1.2), low for G/OTS (I_D/I_G = 0.25) and G/hBN (I_D/I_G = 0.27)	[125]
Silicon wafer, HMDS-treated silicon wafer	Aryl radical addition/4-NBD/0.5 mM in 1 wt.% SDS, 36–40 °C, 7 h	Reactivity: G/SiO_2 (I_D/I_G = 0.45) > G/HMDS (I_D/I_G = 0.30)	[126]
Silicon wafer, *p*Cu, hBN	Radical addition/BPO/10 mM in acetone, 30 min then high-pressure at 80 °C for 25 min	Degree of functionalization: G/SiO_2 > G/hBN > G/*p*Cu	[127]
hBN, mica, silicon wafer, silica nanoparticles (NP)	Oxidation/in Ar and O_2/1.0 L min^{-1} Ar, 0.7 L min^{-1} O_2, 350–600 °C, 2–5 h	Reactivity: G/NP > G/SiO_2 > G/Mica > G/hBN	[54]
TiO_2 film annealed at 800 °C or 400 °C, non-annealed TiO_2	Oxidation/UV light (185 and 254 nm) and ozone/15 min	Significant oxidation for G/annealed TiO_2, higher defect density at 800 °C than 400 °C; No significant oxidation for G/non-annealed TiO_2.	[128]
LIPSS on silicon wafer	Aryl radical addition/4-NBD/5 mM in 1:9 v/v acetonitrile:water, 5 min	Random functionalization on PatA (I_D/I_G = 1.26), periodic functionalization on PatB (I_D/I_G = 1.43)	[129]
Silicon wafer, WS_2, MoS_2	Hydrogenation/hydrogen silsesquioxane (HSQ)/E-beam exposure	High reactivity for G/SiO_2 with high I_D, and low/no reactivity for G/WS_2 and G/MoS_2 (no D band)	[31]
Silicon wafer, MoS_2, hBN	Hydrogenation/0.1 mbar hydrogen plasma (Ar/10% H_2)	G/SiO_2: High hydrogen coverage; G/MoS_2: High hydrogen coverage similar to G/SiO_2; G/hBN: Low hydrogen coverage	[130]
Sb, silicon wafer	Radical addition/DBPO/532 nm laser at 1 mW, ambient conditions	Degree of functionalization: G/SiO_2 > G/Sb	[131]

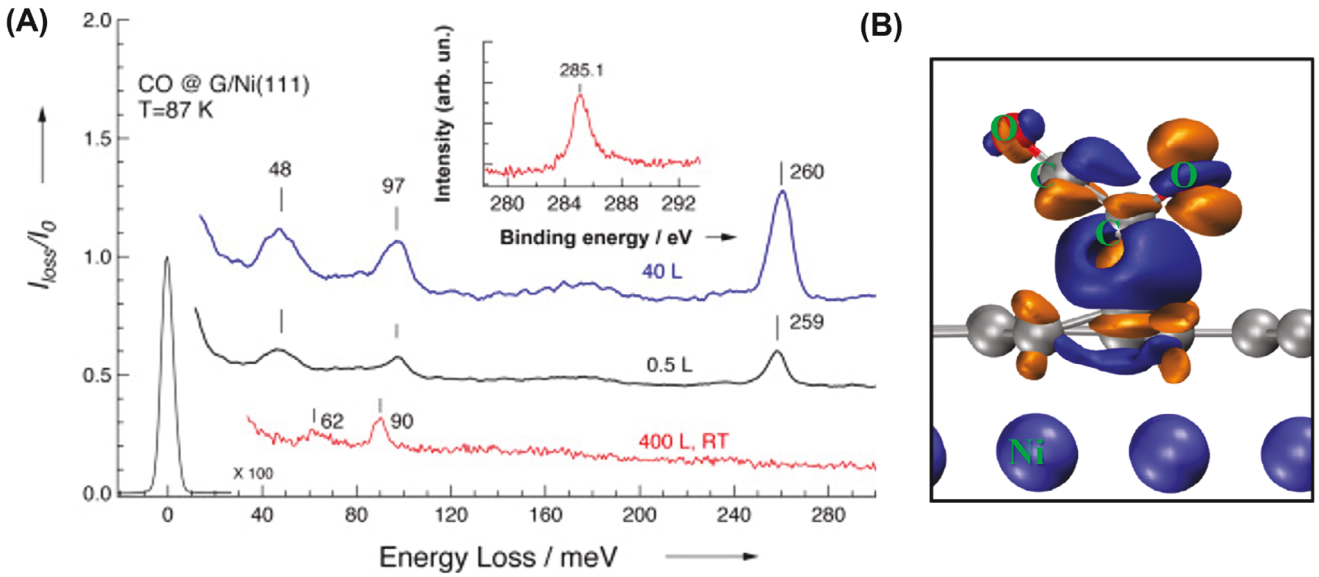

Figure 10. Chemisorption of CO on graphene grown on Ni(111). A) HREEL spectra after exposure of 400 L CO at room temperature (red), 0.5 L (black) or 40 L (blue) CO at 87 K. The peak at 90 meV is the ZO phonon mode of graphene and the peak at 62 meV is the vibrational mode of isolated carbon atoms adsorbed on Ni(111) (red curve). Inset is the XPS C1s spectrum of graphene on Ni(111). B) Charge density difference upon adsorption of ethylene dione (C_2O_2) on graphene supported on Ni(111). Orange regions represent areas of charge accumulation, and blue regions indicate charge depletion, with isosurfaces corresponding to a charge density of ±0.03 $Å^{-3}$. The significant charge redistribution between the C_2O_2 molecule and the underlying graphene carbon atom indicates the formation of a chemical bond. Figure A is reproduced with permission.[112] Copyright 2015, Wiley-VCH. Figure B is reproduced with permission.[122] Copyright 2017, American Institute of Physics.

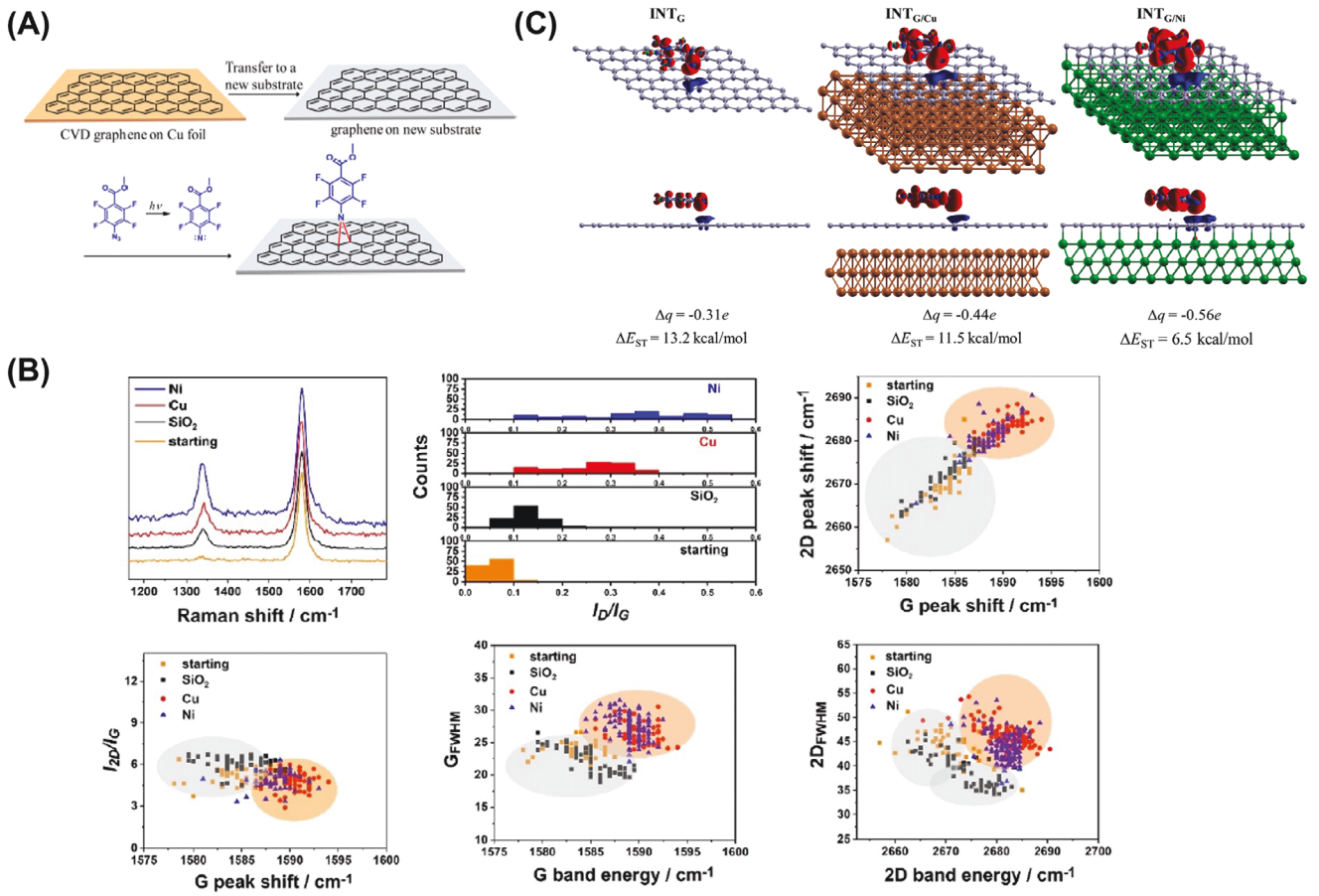

Figure 11. Reaction of PFPA with graphene supported on Ni, Cu and silicon wafer. A) Reaction scheme. B) Respective Raman spectra and analysis of graphene supported on Ni (blue), Cu (red), and SiO_2/Si (black), histograms of I_D/I_G, 2D and G band intensities, positions, and FWHMs of G and 2D bands. (C) DFT calculations showing charge density difference plots, singlet-triplet energy gap (ΔE_{ST}), and charge transfer (Δq). Reproduced with permission.[113] Copyright 2021, Wiley-VCH.

having the highest electron transfer. The singlet-triplet energy gap (ΔE_{ST}) decreases when graphene is supported on metal substrates, at 6.5, 11.5, and 13.2 kcal mol^{-1} for G/Ni, G/Cu, and G/SiO_2/Si, respectively, indicating stabilization of the singlet nitrene by the metal substrates (Figure 11C).

We further investigated the impact of metal substrate in promoting the reaction of graphene in Diels–Alder (DA) reactions.[114] Graphene supported on Ni, Cu and SiO_2/Si was treated with a diene, 2,3-dimethoxy butadiene (DMBD), or a dienophile, maleic anhydride (MAH) (**Figure 12A**). For reaction with DMBD at 50 °C, the D band intensity was the highest for graphene on Ni, followed by Cu, and the lowest for SiO_2/Si. The same trend was observed for reaction with MAH at 100 °C. At all temperatures tested, the reaction followed a pseudo-first-order kinetics (Figure 12B), with the rate of reaction the highest for graphene on Ni, followed by Cu, and lowest on SiO_2/Si. Ni enhanced the reaction rate by a factor of ≈2 compared to SiO_2/Si. The result of MAH was similar to DMBD, with graphene supported on Ni showing higher reactivity than on SiO_2/Si (Figure 12C). DFT calculations are consistent with experimental observations (Figure 12D). The activation energies, referenced to the initial state (IS), are 4.1 and 12.8 kcal mol^{-1} for the reaction of G/Ni with MAH and DMBD, much lower than the reaction of G/Cu with MAH and DMBD at 33.9 and 34.2 kcal mol^{-1}, respectively. Computations also indicate a preference of metal-supported graphene as an electron-rich dienophile in the reaction with electron-deficient dienes in an inverse electron-demand Diels–Alder mechanism.

McBreen and coworkers studied the adsorption of *N*-heterocyclic carbene (NHC) on graphene supported on Pt(111) or Ru(0001) (**Figure 13A**) by measuring the adsorption band of CF_3 in the carbene precursor $(iPr)_2BIMCF_3{\cdot}H_2CO_3$ using reflection absorption infrared spectroscopy (RAIRS).[115] On Pt(111) or Ru(0001), both in-plane (1329 cm^{-1}, 1184 cm^{-1}) and out-of-plane CF_3 (1148 cm^{-1}) modes were observed (Figure 13B), indicating a mix of both vertical and flat-lying adsorption geometries. The NHC adsorbed strongly on graphene supported on either Pt(111) or Ru(0001), however, the out-of-plane CF_3 mode at ≈1148 cm^{-1} was the main peak observed, especially at higher temperature of 350 K. This suggested a flat-lying geometry of the NHC on graphene. The thermal stability of the NHC on graphene/Pt(111) was higher than on graphene/Ru(0001), with the peak at ≈1148 cm^{-1} disappearing at 450 and 400 K, respectively. The author rationalized the

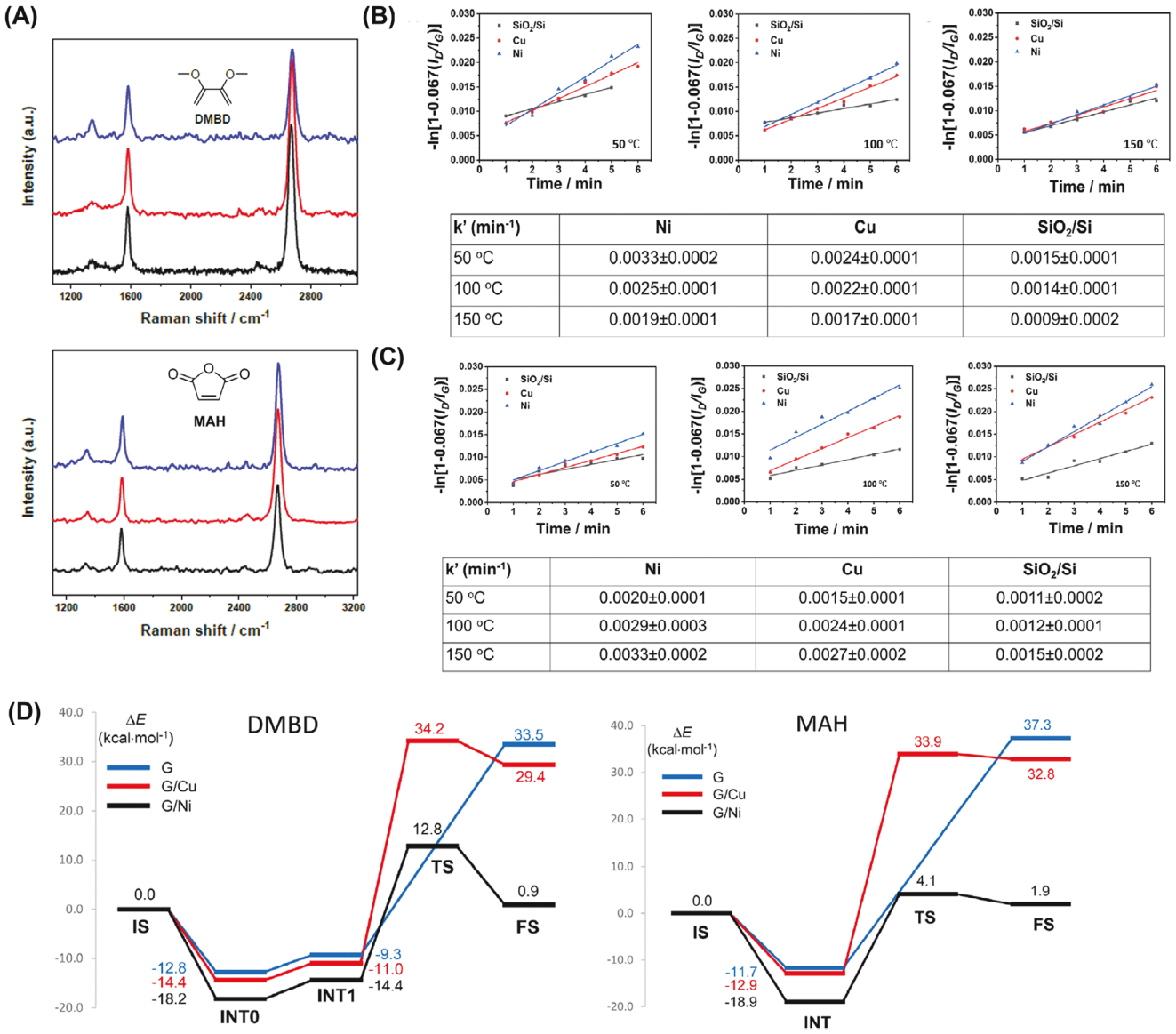

k' (min-1)	Ni	Cu	SiO2/Si
50 °C	0.0033±0.0002	0.0024±0.0001	0.0015±0.0001
100 °C	0.0025±0.0001	0.0022±0.0001	0.0014±0.0001
150 °C	0.0019±0.0001	0.0017±0.0001	0.0009±0.0002

k' (min-1)	Ni	Cu	SiO2/Si
50 °C	0.0020±0.0001	0.0015±0.0001	0.0011±0.0002
100 °C	0.0029±0.0003	0.0024±0.0001	0.0012±0.0001
150 °C	0.0033±0.0002	0.0027±0.0002	0.0015±0.0002

Figure 12. Diels–Alder reaction on substrate-supported graphene. A) Representative Raman spectra for graphene on nickel (G/Ni, blue), copper (G/Cu, red), and silicon wafer (G/SiO_2/Si, black) after reaction with DMBD at 50 °C for 5 min and with MAH at 100 °C for 5 min. B) Plots of $-\ln[1-0.067(I_D/I_G)]$ versus time for the pseudo-first-order reaction kinetics of DMBD with graphene supported on Ni (blue), Cu (red), and silicon wafer (grey) at three different temperatures (50 °C, 100 °C, and 150 °C). C) Plots of $-\ln[1-0.067(I_D/I_G)]$ versus time for the pseudo-first-order reaction kinetics of MAH with graphene supported on Ni (blue), Cu (red), and silicon wafer (grey) at three different temperatures (50 °C, 100 °C, and 150 C). D) DFT calculated energy profiles for the Diels–Alder reaction between graphene and DMBD (left) or MAH (right). IS: Initial state, INT: Lowest energy intermediate, TS: Transition state., FS: Final state. Reproduced with permission.[114] Copyright 2022, Royal Society of Chemistry.

stronger absorption of NHC on graphene/Pt(111) as the NHC being an excellent σ-donor and graphene being *p*-doped on Pt(111) and *n*-doped on Ru(0001). To further confirm that *p*-doping was responsible for the increased absorption, graphene on Ru(0001) was treated with oxygen prior to NHC adsorption. The thermal stability of NHC on graphene/Ru(0001) increased with oxygen intercalation which made it more *p*-doped. This study concluded that NHC adsorption was stronger on the *p*-doped graphene/Pt(111) than the *n*-doped graphene/Ru(0001) and can be further enhanced by increasing *p*-doping in graphene.

Moiré Patterns formed between graphene and metal substrate can also impact the reactivity of graphene (**Figure 14**).[116–118] Hornekær et al. studied the hydrogen adsorption on graphene supported on Ir(111).[116] Figure 14A-a is the STM image of graphene on Ir(111), revealing the characteristic moiré pattern formed from the periodic mismatch between the graphene lattice and the Ir(111) substrate. When graphene was exposed to a very low dose of atomic hydrogen, a number of protrusions appeared on the graphene surface (Figure 14A-b). These protrusions are located at the bright parts of the moiré pattern, suggesting preferential adsorption on these sites. With increasing

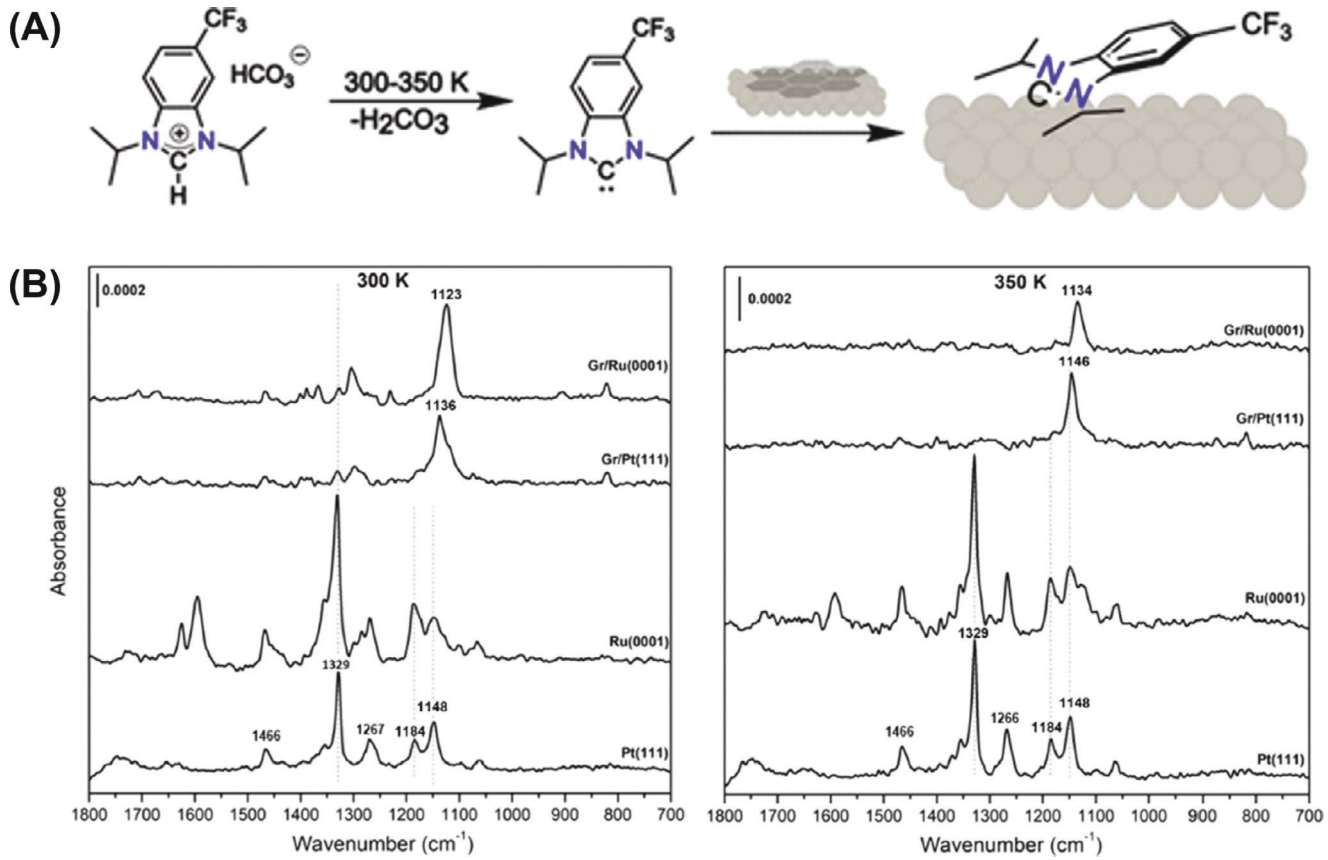

Figure 13. Reaction of metal-supported graphene with NHC. A) NHC reaction on graphene using $(iPr)_2BIMCF_3{\cdot}H_2CO_3$ as the carbene precursor. B) RAIRS spectra comparing adsorption of $(iPr)_2BIMCF_3{\cdot}H_2CO_3$ on graphene/Pt(111) or graphene/Ru(0001) versus directly on Pt(111) or Ru(0001) at 300 K (left), and 350 K (right). If NHC was adsorbed flat-lying on the surface, out-of-plane vibrational bands resulting from the asymmetric CF_3 stretching was observed at ≈1148 cm^{-1}. If NHC was adsorbed vertically on the surface, two in-plane vibrational bands appeared: one ≈1329 cm^{-1} for the symmetric C–CF_3 stretching mode and another ≈1184 cm^{-1} for the asymmetric CF_3 stretching mode. Reproduced with permission.[115] Copyright 2016, American Chemical Society.

exposure time, the hydrogen atoms started to form ring-like structures along the bright parts of the moiré pattern (Figure 14A-c), merged into elongated structures (Figure 14A-d), and further evolved into more extended elongated patterns while preserving the overall moiré periodicity (Figure 14A-e). Fourier transform confirmed the moiré periodicity having the real-space distance of 21.5 Å, which corresponds to the 25 Å × cos(30°) moiré superlattice periodicity (Figure 14A-f). The ARPES revealed a bandgap of 450 meV below the Fermi level when graphene was exposed to a 50 s dose of atomic hydrogen. Computation indicated that hydrogen atoms preferentially formed graphane-like islands in regions of the moiré pattern where conversion of sp^2 to sp^3 led to elimination of the π-band locally and contributed to the bandgap opening observed experimentally.

Berndt et al. investigated the reactivity of graphene on Ir(111) with iron phthalocyanine (FePc).[117] The authors used the DA reaction as a theoretical framework to understand this interaction, although the reaction was considered as non-classical due to the influence of the Ir substrate. Specifically, graphene on Ir(111) exhibits localized "dangling bonds" in its top-fcc moiré registry, which creates reactive sites on the graphene surface. These dangling bonds enable graphene to act like an allyl C3 unit which undergoes a DA-type cycloaddition with a C2 fragment of FePc (Figure 14B-a). STM imaging revealed two configurations of FePc on the graphene surface: a mobile four-lobe state and an immobile three-lobe state (Figure 14B-b). The immobile three-lobe state results from covalent bonding between FePc and specific regions of the graphene, which is further stabilized by the Ir substrate (Figure 14B-c). This bonding induces localized changes in the graphene layer, stabilizing the FePc molecule and altering its appearance in STM images (Figure 14B-d). DFT calculations support the hypothesis, showing that this DA-type cycloaddition stabilizes the FePc-graphene complex and aligns well with the experimental observations, including the orientation and stability of the resulting configuration.

Taking advantage of moiré patterns formed by growing graphene on Ru(0001), Miranda and coworkers covalently functionalized graphene with cyanomethyl radicals ($\bullet CH_2CN$) produced from homolytic cleaving acetonitrile by electron bombardment, and showed atomic-level selectivity and spatial periodicity.[118] STM images taken at different bias voltages revealed the bright bumps corresponding to the adsorption of $\bullet CH_2CN$ located predominantly at the HCP-Top sites, marked with white circles in Figure 14C. The differential conductance

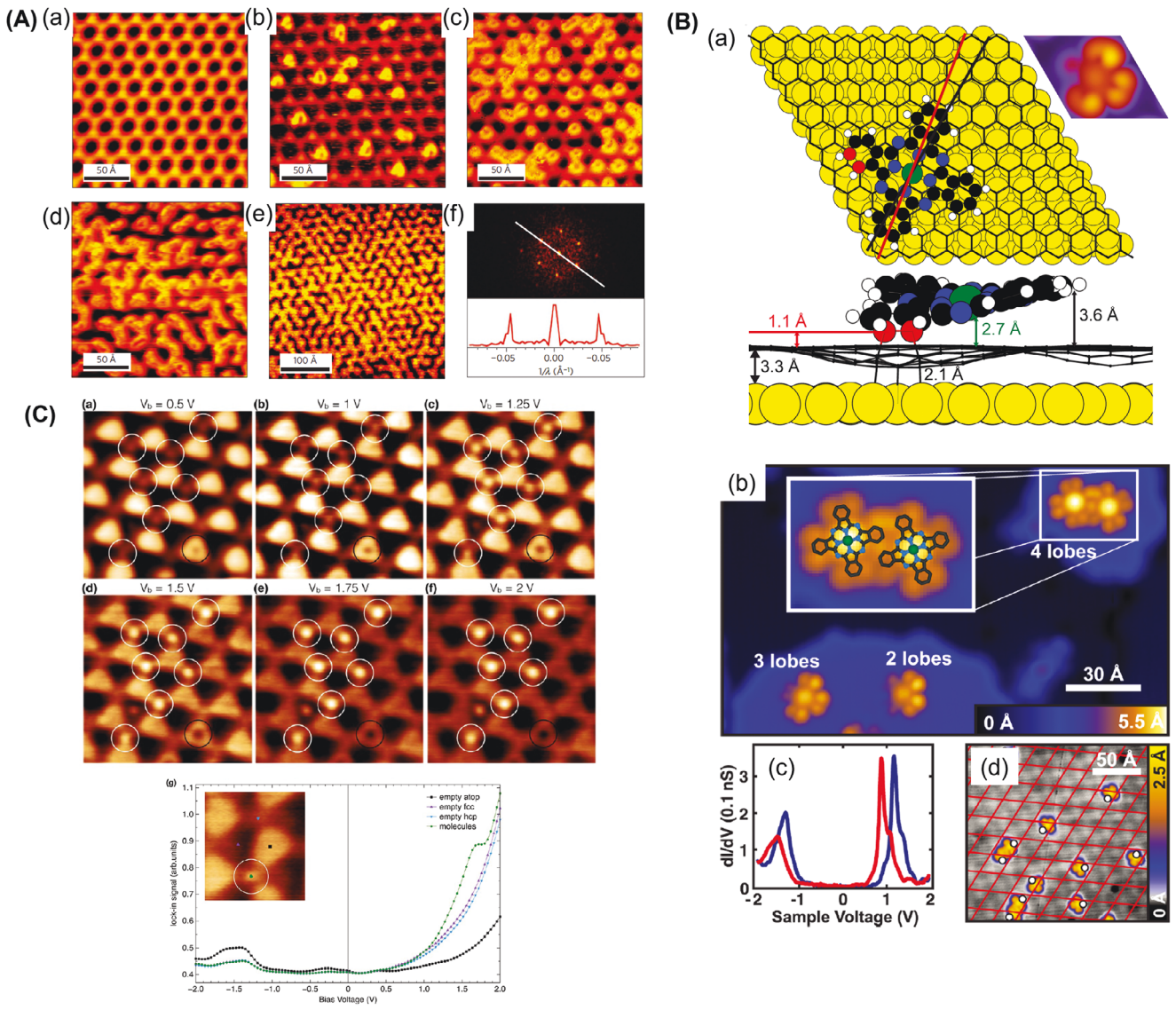

Figure 14. Effect of moiré patterns on graphene reactivity. A) Hydrogen adsorption on graphene/Ir(111). A-a) Clean graphene surface showing the moiré pattern. A-b) Initial hydrogen adsorption sites as protrusions on the bright parts of the moiré pattern. A-c) Ring-like hydrogen structures formed after 15 s of hydrogen exposure. A-d) The rings merged into elongated structures after 30 s. A-e) Further evolution into extended patterns after 50 s, maintaining moiré periodicity. A-f) Fourier transform of A-e). B) Reactivity of FePc on graphene supported on Ir(111). B-a) Optimized structure of the proposed DA-type cycloadduct C3-Pc(5,6) formed between FePc and graphene on Ir(111). The inset is a simulated STM image of the moiré cell. B-b) STM image of FePc on graphene. The inset is a four-lobed FePc dimer with an overlaid molecular structure. B-c) Differential conductance (dI/dV) spectra measured at the centers of four-lobed (blue) and three-lobed (red) FePc molecules. B-d) STM image showing the distribution of three-lobed FePc molecules across the graphene-Ir moiré pattern. C) Selective functionalization of graphene on Ru(0001) with cyanomethyl radicals. C-a-f) STM images (10×10 nm^2) after exposure to 180 Langmuirs of acetonitrile at 300 K, occurring primarily at HCP-Top sites (white circles) with fewer at FCC-Top sites. Black circles are graphene point defects. C-g) Differential conductance (dI/dV) curves at 80 K showing an additional peak at +1.6 eV, further supporting selective functionalization at HCP-Top sites. Figure A is reproduced with permission.[116] Copyright 2010, Springer. Figure B is reproduced with permission.[117] Copyright 2015, American Chemical Society. Figure C is reproduced with permission.[118] Copyright 2016, American Chemical Society.

curves provided additional evidence of selective functionalization. The presence of the LUMO peak at +1.6 eV in the green curve indicated covalent bonding of the cyanomethyl radicals at the HCP-Top sites (Figure 14C-g). For graphene on Ir(111), no molecular attachment was observed when exposed to acetonitrile. The authors attributed this to weak interaction between graphene and Ir(111), although graphene grown on Ir(111) also exhibits a moiré pattern similar to that on Ru(0001).

The Ruoff group examined the reactivity of graphene on Cu(111) and Cu(115) in electrochemical functionalization.[119] The electrochemical reaction involved applying a negative potential to graphene in the presence of 4-iodoaniline. A three-electrode electrochemical cell was used, with graphene/Cu(111) as the working electrode, $Ag/AgNO_3$ as the reference electrode, and a Pt foil as the counter electrode. Results in **Figure 15**A showed that graphene on Cu(115) was more reactive and had

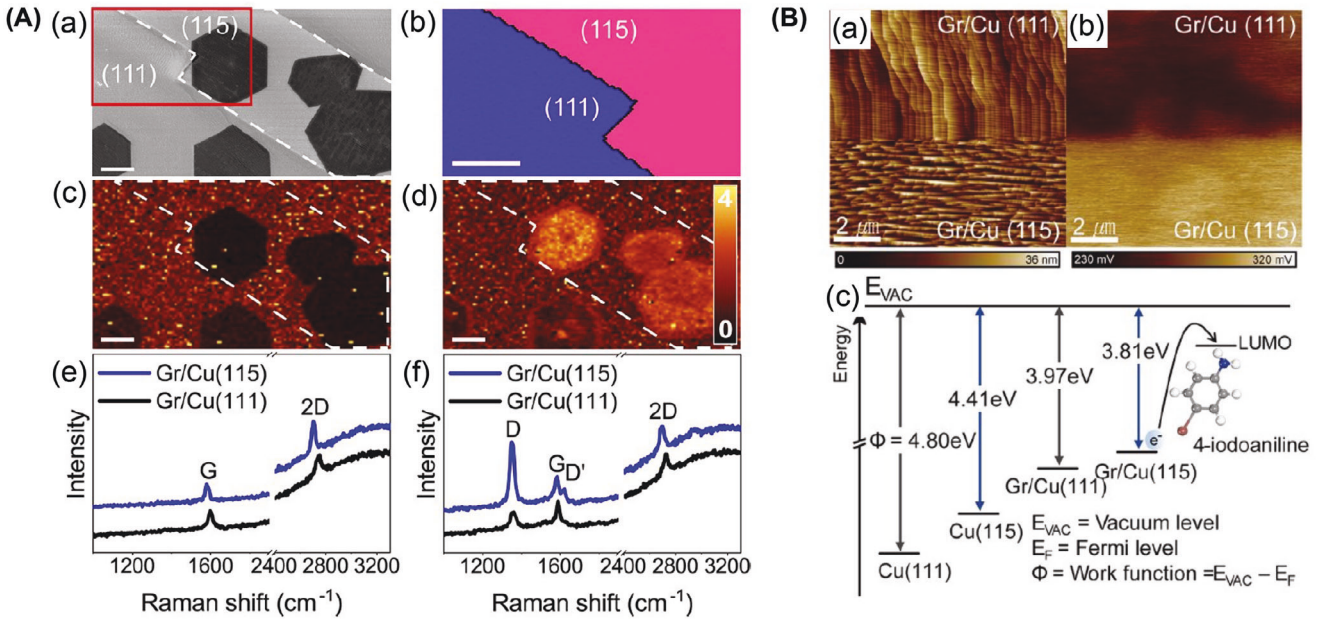

Figure 15. Electrochemical reaction of graphene on Cu(111) and Cu(115). A-a) SEM image of graphene islands on Cu(111) and Cu(115); A-b) EBSD maps of Cu(111) and Cu(115) surfaces; A-c,d) I_D/I_G map before (left) and after (right) electrochemical reaction; A-e,f) Raman spectra of graphene before (left) and after reaction (right). B-a) AFM height map and B-b) KPFM potential distribution of graphene on Cu(111) and Cu(115); B-c) Calculated work functions of Cu(111), Cu(115), Gr/Cu(111), and Gr/Cu(115). Reproduced with permission.[119] Copyright 2016, American Chemical Society.

a higher degree of functionalization than graphene on Cu(111). After the reaction, the D band appeared and I_D/I_G increased significantly, especially in regions of graphene on Cu(115) (Figure 15A-f). Graphene on Cu(111) and Cu(115) had different topographies due to the underlying step bunching on the copper substrates (Figure 15B-a). Kelvin probe force microscopy (KPFM) revealed a potential distribution corresponding to AFM imaging (Figure 15B-b). Work function calculations showed a higher Fermi energy for graphene on Cu(115) compared to Cu(111) (Figure 15B-c), indicating greater electron doping of graphene by Cu(115). This increased electron doping results in a lower energy barrier for electron transfer to 4-iodoaniline.

Liu and coworkers reported two studies on how substrate affected the oxidation of graphene photochemically[120] or thermally.[121] Photochemical oxidation was done by ultraviolet-ozone (UVO) treatment. After 30 min of UVO treatment, the intensity of the G peak decreased significantly and the 2D peak nearly disappeared (**Figure 16**A-b), indicating structural degradation of graphene. The ratio of the area of the D peak to the G peak (A_D/A_G) of asgraphene at 0.10 ± 0.04 increased to 1.40 ± 0.08 after UVO treatment. Structural degradation was much less if UVO treatment was done directly on CVD graphene grown on Cu foil. Both G peak and 2D peaks retained high intensities similar to the untreated graphene (Figure 16A-c), with an A_D/A_G of 1.00 ± 0.12. However, if the CVD graphene was transferred to an annealed Cu foil and then subjected to UVO, the intensities of G and 2D peaks decreased along with peak broadening (Figure 16A-d), and A_D/A_G increased to 1.51 ± 0.08 after UVO treatment. The XPS results were consistent with the Raman data, showing that graphene on silicon wafer underwent the highest degree of oxidation, with the highest intensity of O1s peak and a lowest intensity of C1s peak, whereas CVD graphene remained on its growth substrate of Cu foil exhibited the least oxidation and graphene transferred onto annealed Cu foil showed an intermediate level of oxidation. The authors attributed this to the adhesion energy between graphene and substrate, suggesting that stronger adhesion reduces the susceptibility of graphene to UVO oxidation. On the other hand, the Liu group found that freshly prepared CVD graphene on Cu foil (Figure 16C-a) and graphene transferred to Cu (Figure 16C-b) were almost completely oxidized after annealing at 600 °C for 2 h even under trace amount of oxygen (<3 ppm in argon).[121] CVD graphene on Ni (Figure 16C-c) or graphene transferred to silicon wafer (Figure 16C-d) were less oxidized, with G and 2D peaks still visible after annealing. The author attributed the high oxidation of graphene on Cu to the formation of copper oxide between graphene and copper, which catalyzed the oxidative degradation of graphene.

3.3.2. Impact of Non-Metal Substrates on Charge Doping in Graphene and Its Reactivity

Charge doping in graphene caused by non-metal substrates results from interactions that modify electronic properties of graphene through charge transfer, impurities, and surface chemistry. Non-metal substrates such as SiO_2,[125] sapphire,[125] and mica[54] have been used to alter the doping level in graphene through interactions with graphene. SAMs provide an additional method for controlling substrate-induced doping, by altering substrate surface characteristics. Graphene on SiO_2 substrates has reported high reactivity toward radical addition reactions,[132–137] thermal oxidation,[54] and hydrogenation,[31,130] mainly due to charge puddles within graphene. Enhanced reactivity was also observed for graphene toward radical addition on

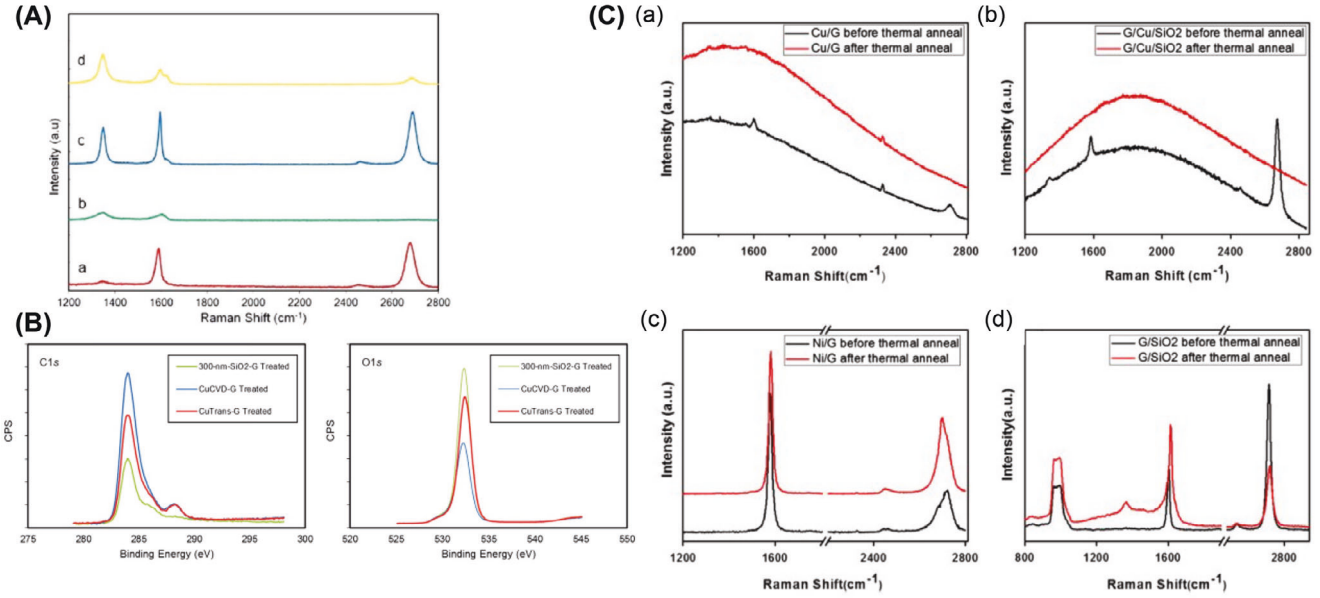

Figure 16. Photochemical and thermal oxidation of substrate-supported graphene. A) Raman spectra of graphene on silicon wafer A-a) before and A-b) after 30 min of UVO treatment. A-c) CVD graphene grown on Cu foil after 30 min of UVO. A-d) Graphene transferred onto an annealed copper after 30 min of UVO. Samples in A-c) and A-d) were transferred to silicon wafers before Raman characterization. (B) XPS C1s and O1s peaks of UVO-treated graphene samples. C) Raman spectra of C-a) CVD graphene grown on Cu, C-b) CVD graphene transferred onto Cu-coated silicon wafer, C-c) multi-layer CVD graphene grown on nickel, C-d) CVD graphene transferred onto silicon wafer before (black) and after (red) annealing in Ar (< 3 ppm O_2) at 600 °C for 2 h. Figures A and B are reproduced with permission.[120] Copyright, 2016, Royal Society of Chemistry. Figure C is reproduced with permission.[121] Copyright 2015, Elsevier.

sapphire,[125] toward thermal oxidation on mica,[54] and toward UV-ozone oxidation on crystalline TiO_2.[128]

On SiO_2 substrates, environmental impurities, possibly from exposure to air and H_2O trapped at the graphene-SiO_2 interface, can create local electric fields leading to fluctuations in the charge density. These fluctuations can result in regions of high electron density (electron puddles) and regions of high hole density (hole puddles) in graphene.[132–137] By mapping the local Dirac point in graphene on a SiO_2 substrate using STM and spectroscopy, Crommie et al. found that charge density fluctuations are caused not by topographic corrugations but by charge-donating impurities located beneath the graphene.[135] These impurities created electron-rich and hole-rich regions known as "charge puddles" with sizes averaging ≈20 nm and contributed an average charge fluctuation of ≈0.07 ± 0.03e per impurity. Regions of different charge densities create areas of varying electron or hole concentrations across the graphene surface, which has been effectively leveraged to modulate the reactivity of graphene at the nanoscale.

Sapphire can tune the doping level in graphene primarily through its surface, particularly through water molecules at the graphene/substrate interface.[138] When graphene is placed on single-phase, Al-terminated (hydrophilic) sapphire substrates, the Raman G band shifted to higher frequency, indicating hole doping induced by water layers attracted to the hydrophilic surface. In contrast, phase-separated sapphire substrates have both Al-terminated (hydrophilic) and O-terminated (hydrophobic) domains, leading to two distinct peaks in the G band: G1-peak (1587 cm^{-1}) from the O-terminated domain and G2-peak (1593 cm^{-1}) from the Al-terminated domain. The Al-terminated domains cause more significant hole doping due to the higher water adsorption, whereas O-terminated hydrophobic domains show smaller shift in the G band frequency and lower doping. This variation in doping levels between domains allows sapphire substrates to locally modulate the doping level in graphene based on their hydrophilic or hydrophobic surface characteristics.

Mica tunes the doping level in graphene primarily through interfacial charge transfer. In direct contact with mica, graphene experiences *p*-doping, leading to a significant hole density of $\approx 9 \times 10^{12}$ cm^{-2}.[139] This doping effect was attributed to electron transfer from graphene to mica, raising the Fermi level. However, when a single bilayer of water (≈0.4 nm thick) is present at the interface, this charge transfer is largely blocked, reducing the doping effect. Graphene on mica exhibits a more uniform charge distribution compared to graphene on SiO_2.

SAMs offer a versatile way to modify substrates and tune the doping level in graphene by introducing different functional groups at the graphene-substrate interface, which either donate or withdraw electrons to modulate the charge carrier concentration in graphene.[37,125,126] For instance, F-SAMs prepared by modifying SiO_2 surface with perfluorooctyltriethoxysilane induce *p*-type doping by creating a partial positive charge near graphene, whereas H_2N-SAMs prepared by treating SiO_2 with 3-aminopropyltriethoxysilane resulted in *n*-type doping by donating electrons to graphene.[140] On the other hand, nonpolar alkyl-terminated SAMs can remove or significantly decrease impurities from the substrates. This leads to reduced charge doping and lower reactivity of graphene.[125,140–142] Alkyl-terminated SAMs have also been used to minimize charge inhomogeneity in graphene by screening the charge puddles.[125,126]

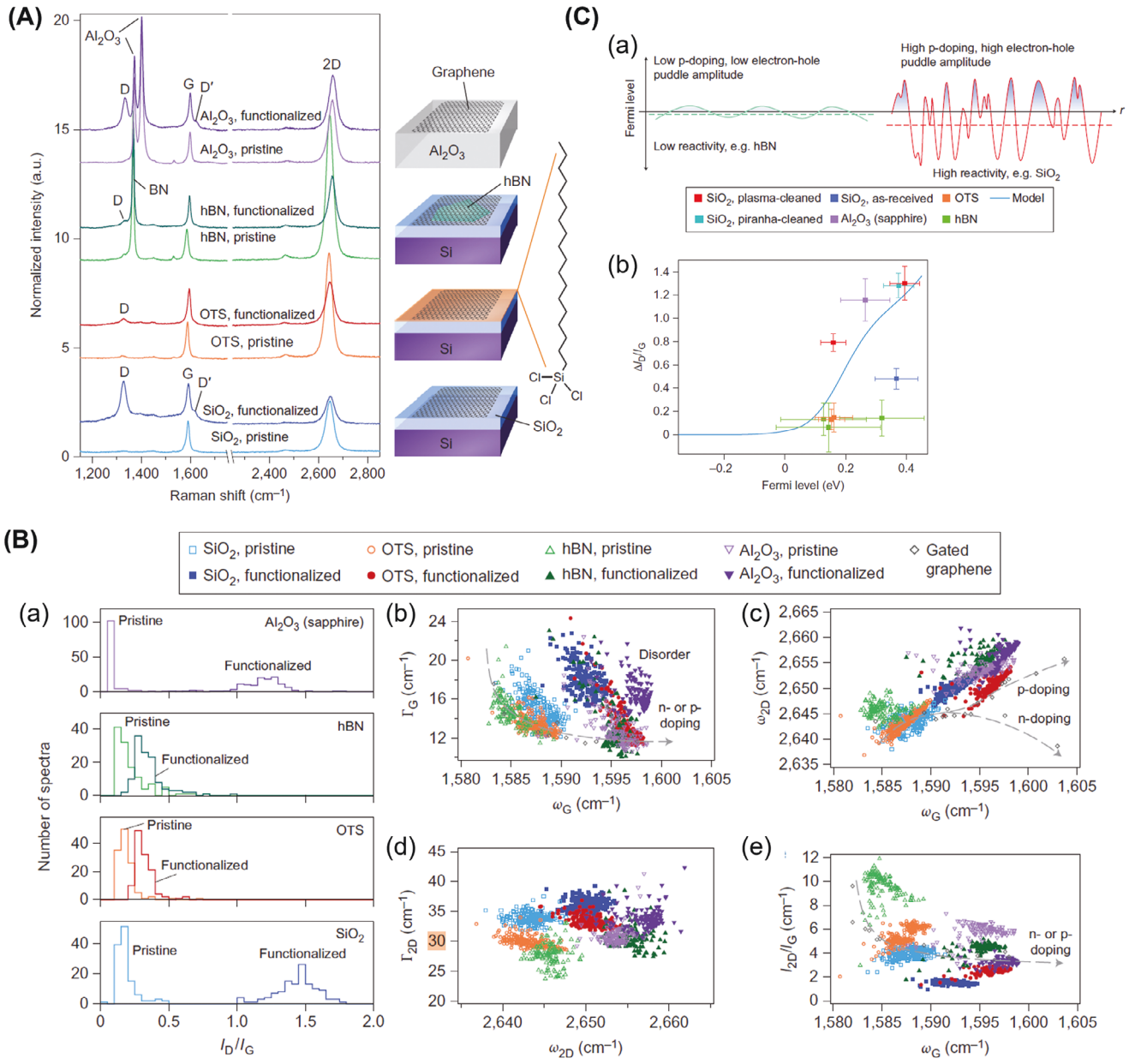

Figure 17. Substrate-induced charge puddles and effects on the reaction of graphene with 4-NBD. A) Raman spectra of graphene on different substrates before and after reaction with 4-NBD. B-a) I_D/I_G histograms of substrate-supported graphene before and after diazonium functionalization. B-b–e) Raman scatter plots. C) Charge puddle amplitude on different substrates and impact on I_D/I_G. Reproduced with permission.[125] Copyright 2012, Springer.

The Strano group investigated how different substrates influence the reactivity of graphene in the reaction with 4-NBD.[125] The authors used oxygen plasma-treated silicon wafer (SiO_2), single-crystal α-Al_2O_3, octadecyltrichlorosilane (OTS)-functionalized silicon wafer, and single-crystal hexagonal boron nitride (hBN) deposited on silicon wafer as the substrates, and found that SiO_2 and Al_2O_3 enhanced while hBN and OTS decreased the reactivity of graphene, with I_D/I_G of 1.4, 1.2, 0.25, and 0.27 for the four substrates, respectively (**Figure** 17A,B-a). After functionalization, the G peak position (ω_G) upshifted for graphene supported on all substrates, indicating increased doping (Figure 17B-b,c). The FWHM of the G peak (Γ_G) was greater for graphene on SiO_2 and Al_2O_3, indicating higher levels of disorder on these two substrates (Figure 17B-b). A scatter plot of 2D peak position (ω_{2D}) versus G peak position (ω_G) showed that unfunctionalized graphene was slightly *p*-doped, with hBN showing lower and Al_2O_3 showing higher doping (Figure 17B-c). After functionalization, graphene on all substrates shifted further into *p*-doping. Scatter plot of 2D peak FWHM (Γ_{2D}) versus 2D peak position (ω_{2D}) (Figure 17B-d) showed that the 2D peak position changed in opposite directions for electron and hole doping (Figure 17B-c). The author suggested that a higher Γ_{2D} value

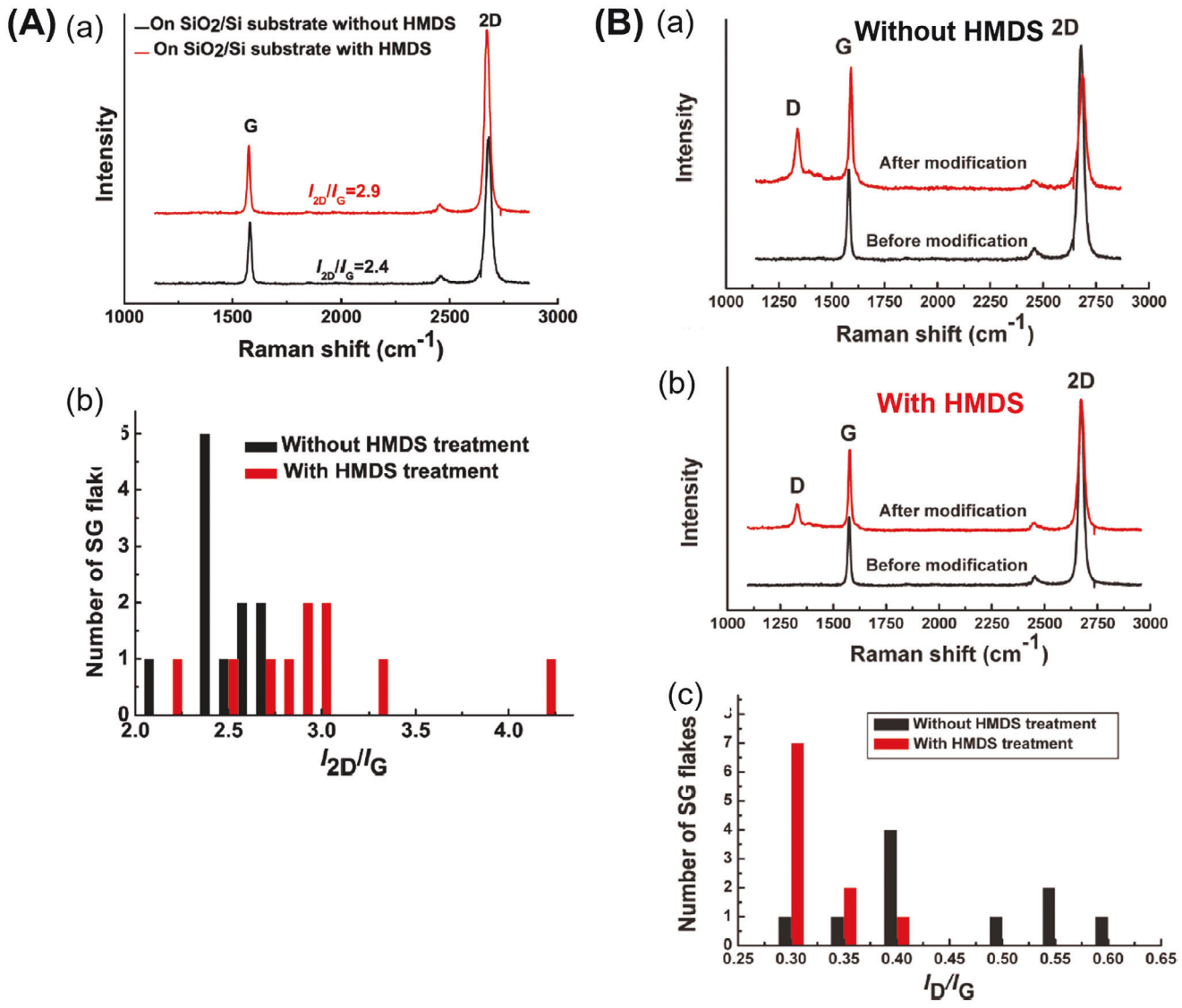

Figure 18. Passivation of SiO_2 with HMDS reduced reactivity of graphene with 4-NBD. A-a) Raman spectra and A-b) I_{2D}/I_G of graphene on SiO_2/Si with and without HMDS treatment. B) Raman spectra of graphene on SiO_2 B-a) without and B-b) with HMDS treatment before and after reaction with 4-NBD, B-c) I_D/I_G. Reproduced with permission.[126] Copyright 2016, American Chemical Society.

was correlated with greater charge fluctuation, with graphene on SiO_2 having the highest Γ_{2D}, whereas graphene on hBN the lowest. The decrease in I_{2D}/I_G and increase in Γ_G was suggested to be from increased doping (Figure 17B-e). The authors further modeled the reactivity based on the electron-transfer theory, proposing that local charge puddles created by substrate interactions are responsible for the enhanced reactivity (Figure 17C). Substrates like SiO_2 introduce more charge inhomogeneity, thereby creating local n-doped regions that enhance graphene reactivity. Leveraging this substrate effect, the team fabricated OTS patterns on SiO_2, and carried out the reaction on graphene to achieve micrometer-scale spatial control of reactivity.

Tanigaki et al. also reported that charge puddles affected the reactivity of graphene with 4-NBD.[126] The authors hypothesized that passivation of SiO_2 with hexamethyldisilazane (HMDS) would block the surface Si-OH groups and reduce ionizable impurities such as Na^+ ions within the SiO_2 layer, resulting in fewer charge puddles in graphene. Indeed, graphene on HMDS-treated substrate showed a shift in the 2D band to lower frequency (**Figure 18**A-a), indicating lower doping than graphene on untreated SiO_2. I_{2D}/I_G was > 2.7 for graphene on HMDS-treated substrates and 2.4–2.7 for graphene on untreated substrates (Figure 18A-b). After reaction with 4-NBD, the average I_D/I_G was ≈0.30 for graphene on HMDS-treated, lower than ≈0.45 for graphene on the un-treated substrate (Figure 18B).

Gao et al. employed charge puddles to modulate the reactivity of graphene toward dibenzoyl peroxide (DBPO) via a radical mechanism (**Figure 19**A). Three substrates were tested: SiO_2, copper, and hBN. Before the reaction, graphene showed the highest doping on SiO_2, moderate doping on copper, and the least doping on hBN with I_{2D}/I_G of 3.62, 4.02, and 5.74, respectively (Figure 19B-a). After the reaction, the D band was the

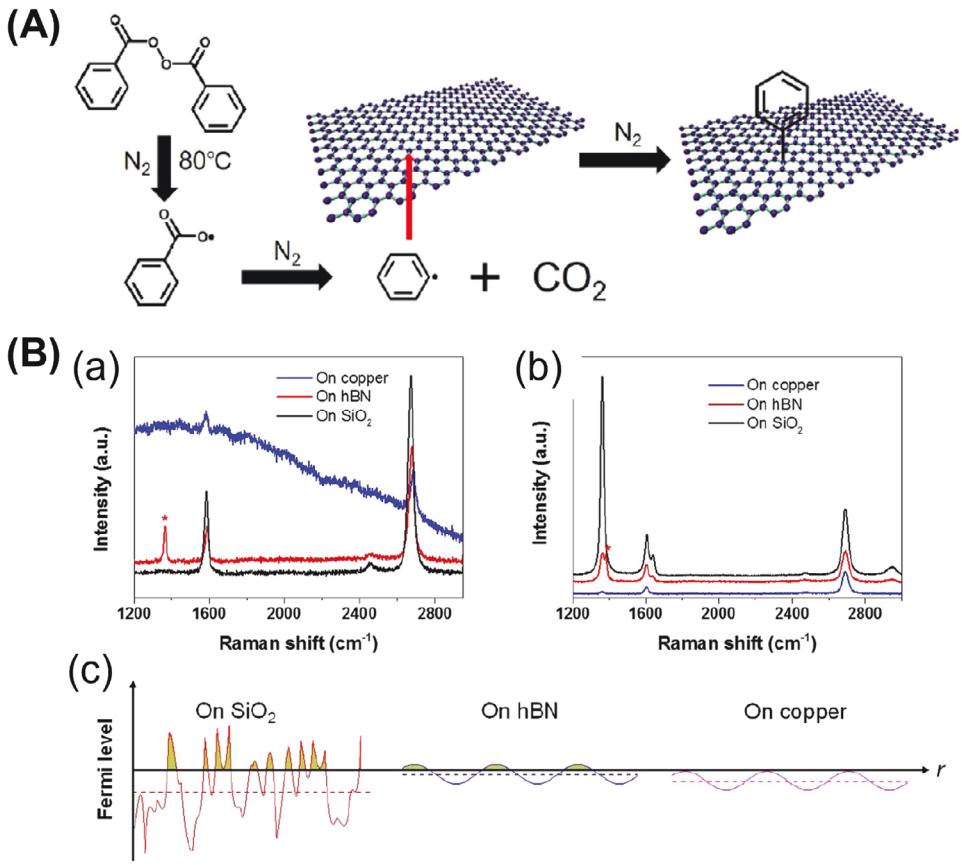

Figure 19. Effect of substrate-induced charge puddles on the reactivity of graphene toward free radical reaction. A) Reaction of graphene with phenyl radicals generated from BPO. B) Raman spectra of graphene on SiO_2, hBN, or copper B-a) before and B-b) after reaction. B-c) Electron-hole charge fluctuation on SiO_2, hBN, and copper. Reproduced with permission.[127] Copyright 2016, Springer.

most intense for graphene on SiO_2, much weaker on hBN, and the weakest on copper (Figure 19B-b). The reactivity was correlated with substrate-dependent electron-hole charge fluctuations (Figure 19B-c). Graphene on SiO_2 is *p*-doped and has the largest electron-hole charge fluctuation. Graphene on hBN or copper is weakly *p*-doped and has small electron-hole fluctuations.

Cullen and coworkers investigated the thermal oxidative reactivity of graphene on different substrates, finding that charge inhomogeneity rather than surface roughness affected the reactivity.[54] Substrates included mica, hBN, silicon wafer (SiO_2), and SiO_2 nanoparticles (NPs). These substrates have different surface roughness, with mica as the smoothest, followed by hBN and SiO_2, while NPs gave the roughest surface (**Figure 20**A). Graphene on hBN, a low-charge impurity substrate, exhibited no etching after oxidation at up to 550 °C (Figure 20B). Raman analysis confirmed a small G-band shift from 1580 to 1585 cm^{-1} in graphene on hBN, showing minimal doping, and no D-band was observed, indicating the absence of oxidation-induced defects (Figure 20C). In contrast, graphene on SiO_2 and mica, substrates with higher charge impurities, showed marked reactivity. For graphene on SiO_2, the G-band shifted from 1582 to 1603 cm^{-1} after oxidation at 500 °C, corresponding to a hole concentration of $\approx 2 \times 10^{13}$ cm^{-2}, and the D-band appeared due to defect formation. Similarly, graphene on mica exhibited significant hole doping and etching, evidenced by D-band activation and a comparable G-band shift. The authors also compared bilayer graphene (BLG) on SiO_2 nanoparticles which is a rougher substrate and found that while single-layer graphene (SLG) exhibited a strong D-peak after oxidation at 500 °C, BLG did not, despite the rough substrate (Figure 20D). This demonstrates that increased charge disorder in SLG, not roughness, enhances oxidative reactivity.

Park et al. investigated how substrates affected the UVO oxidation of graphene, showing a strong dependence on substrate type and crystallinity.[128] Graphene on TiO_2, especially when annealed to achieve high anatase crystallinity, exhibited significantly enhanced oxidation compared to graphene on SiO_2. After 15 min of UVO exposure, graphene on anatase TiO_2 showed a marked increase in I_D/I_G, while graphene on amorphous TiO_2 and SiO_2 displayed minimal changes in I_D/I_G (**Figure 21**A). This substrate-dependent reactivity is attributed to charge transfer. In amorphous TiO_2, defect sites such as impurities, dangling bonds, and microvoids promote electron-hole recombination. Crystalline TiO_2 has fewer defects, allowing photoexcited holes to transfer more effectively to graphene and facilitate oxidation. The authors further demonstrated controlled UVO oxidation of graphene on substrates patterned with TiO_2 and SiO_2 (Figure 21B-a). Graphene on TiO_2 oxidized rapidly under UVO, showing I_D/I_G up to 3, while graphene on SiO_2 remained stable with $I_D/I_G \approx 0.3$ (Figure 21B-b–d).

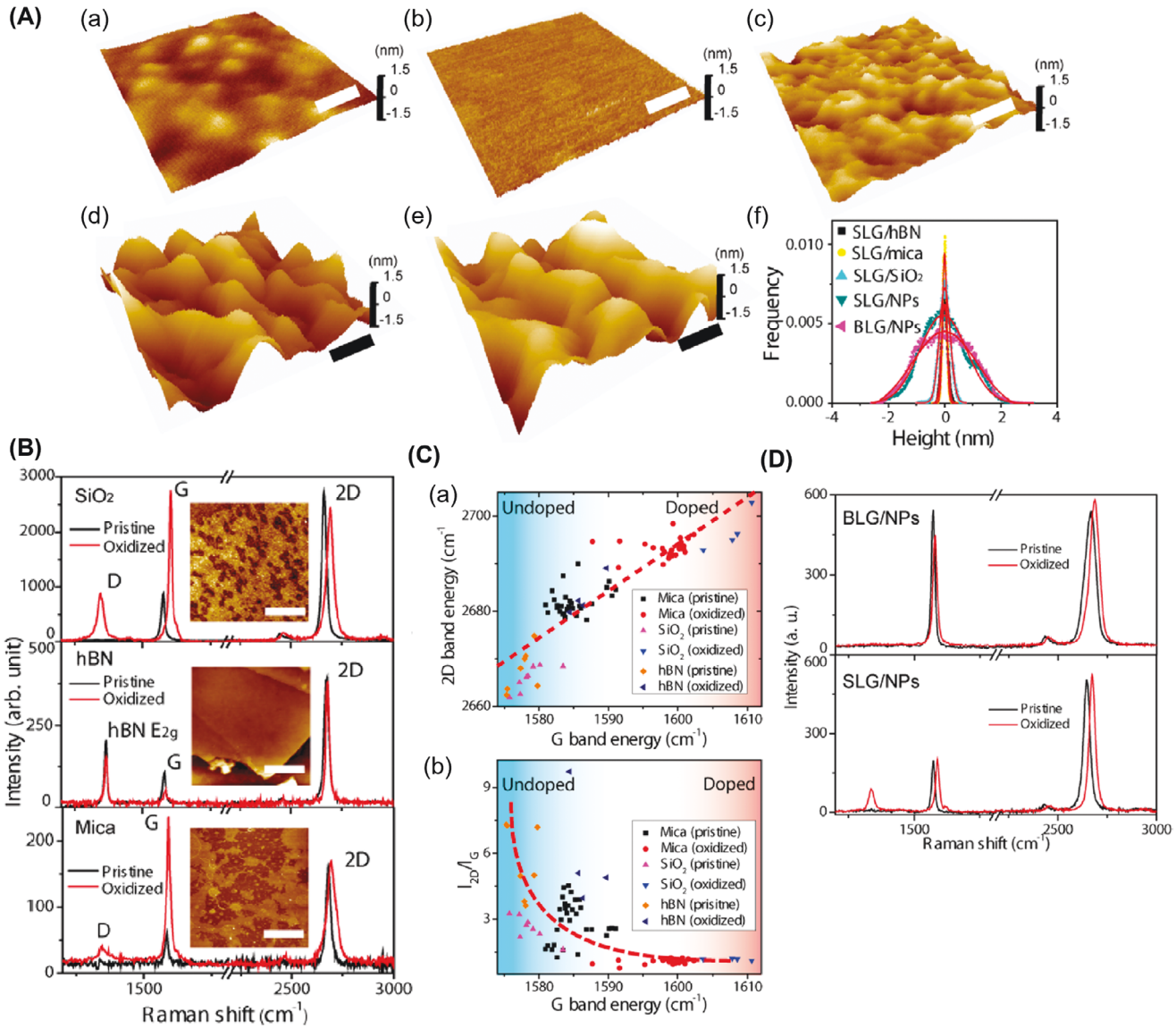

Figure 20. Thermal oxidation of substrate-supported graphene. A) AFM images of SLG supported on different substrates: A-a) hBN, (b) mica, (A-c) SiO_2/Si, A-d) SiO_2 nanoparticle thin film, and (e) BLG on the SiO_2 nanoparticle thin film. (f) Height histograms corresponding to the AFM images in panels (a-e). B) Raman spectra of SLG supported on SiO_2, hBN, and mica, before and after heating in Ar/O_2 at 500 °C for 2 h. Insets are AFM images of SLG on each substrate after oxidation. C) Raman 2D band energy versus G band energy, and I_{2D}/I_G versus G band energy of SLG on mica, hBN, and SiO_2 before and after oxidation. D) Raman spectra of BLG and SLG on SiO_2 nanoparticles before and after oxidation. Reproduced with permission.[54] Copyright 2012, American Chemical Society.

Kalbáč and coworkers investigated how laser-induced periodic surface structures (LIPSS) on SiO_2/Si substrates modulated the doping level in graphene and influenced its reactivity with 4-NBD.[129] LIPSS patterns were created using femtosecond and picosecond laser irradiation at varied fluences and pulse overlaps, resulting in distinct structural patterns. Both strain and doping were observed in graphene on these substrates. Strain levels for graphene on both the shallow LIPSS structure (PatA) and the more protruded structure (PatB) were similar, at less than −0.1% (**Figure** 22B-e,j left panel), however, doping levels differed significantly. On PatA (Figure 22A-c), graphene conformed to the periodic wrinkles (Figure 22A-a,b) and showed a homogeneous doping of 2.88×10^{12} cm^{-2} (Figure 22B-e, right panel). In contrast, on PatB which had more pronounced protrusions from underlying periodic structures (Figure 22A-f), graphene adapted to the smooth bump topography (Figure 22A-d,e) and showed a periodic doping from 4.5×10^{12} to 6.5×10^{12} cm^{-2} (Figure 22B-j, right panel). This variation is attributed to p++-doped silicon deposits beneath the oxide layer, creating periodic electron density aligned with the LIPSS. These substrate-induced doping variations led to different reactivity of graphene in the reaction with 4-NBD. For graphene on PatA, I_D/I_G was uniformly distributed at ≈1.26 (Figure 22C-c), suggesting consistent reactivity across the surface. In contrast, graphene on PatB

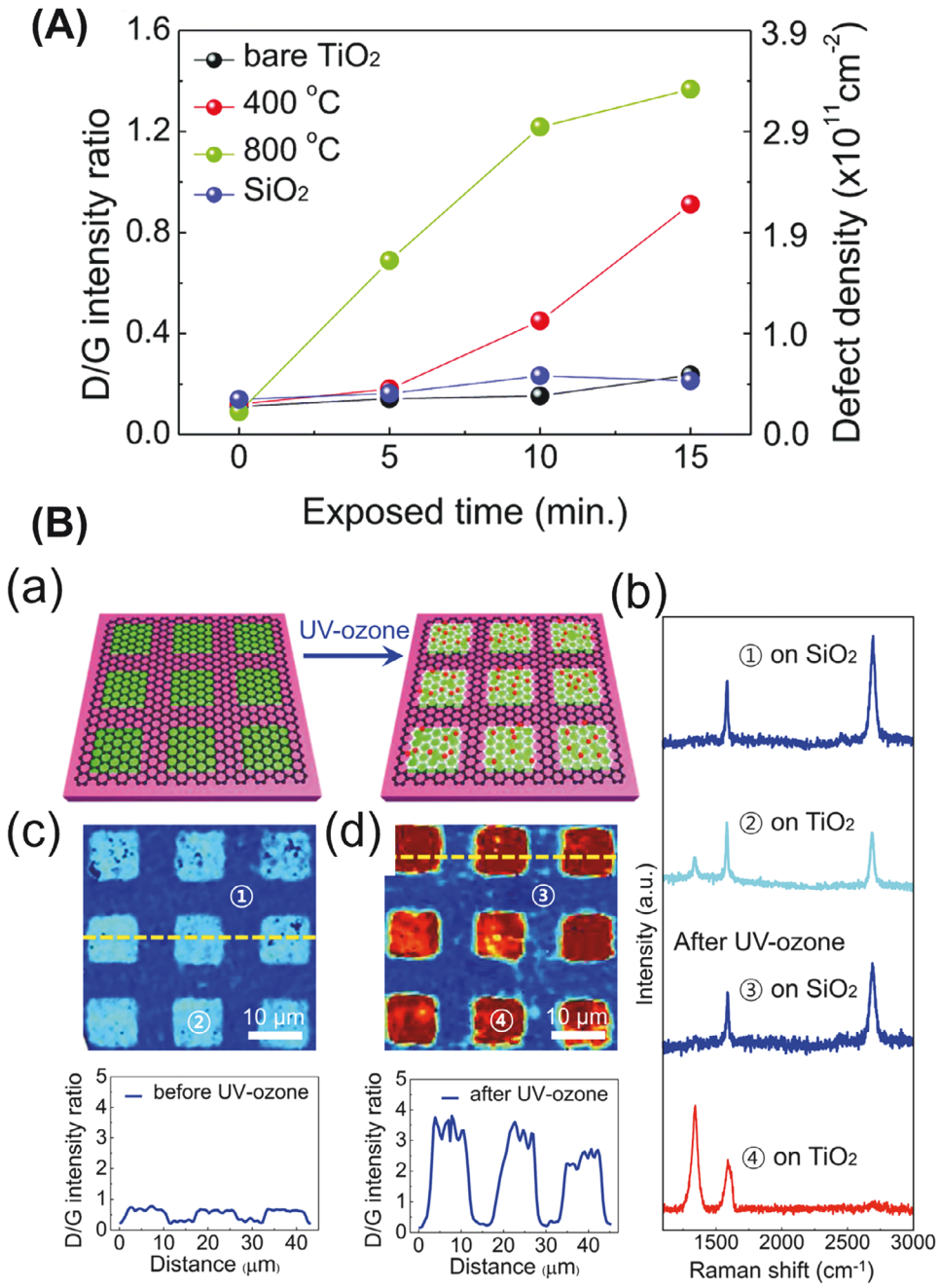

Figure 21. UVO oxidation of graphene on SiO_2, amorphous or annealed crystalline TiO_2. A) Raman I_D/I_G and defect density as a function of UVO exposure time. B-a) Oxidation of graphene on patterned substrates of SiO_2 and TiO_2. B-b) Raman spectra of graphene on patterned surface. The numbers 1–4 corresponded to the positions in B-c) and B-d). Raman I_D/I_G maps and intensities (B-c) before and (B-d) after UVO. Reproduced with permission.[128] Copyright 2016, Royal Society of Chemistry.

showed periodic I_D/I_G with a median of 1.43 (Figure 22C-f) and a periodicity of 1 μm, matching the LIPSS pattern and indicating enhanced functionalization in the doped regions. This periodic modulation of I_D/I_G was not observed outside the periodically structured area (green line,Figure 22C-g), confirming that the LIPSS specifically influenced reactivity within the patterned regions.

3.3.3. 2D Materials Reduce Charge Doping

Graphene on other 2D materials like hBN, MoS_2, and WS_2 can form vdW heterostructures.[143,144] It has been observed that charge fluctuations in graphene on hBN were significantly reduced compared to graphene on SiO_2.[145,146] Annealing in H_2/Ar enhanced carrier mobility without significant doping,

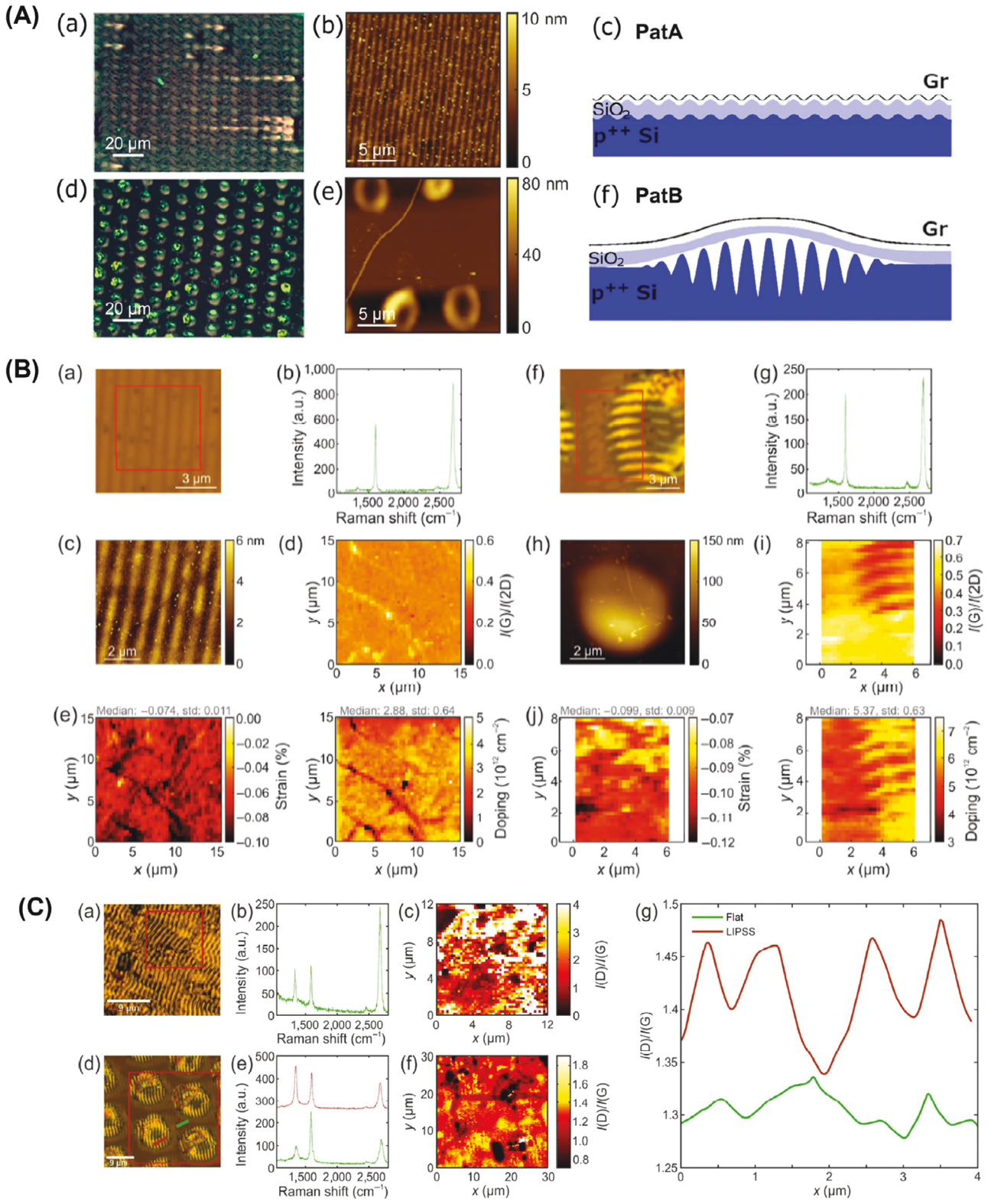

Figure 22. Periodic doping in graphene on LIPSS structures and reaction with 4-NBD. A) Optical images, AFM images, and schematic of (A-a – A-c) PatA, and (A-d – A-f) PatB. B) Optical images, Raman spectra, AFM images, Raman I_D/I_G maps and strain/doping distributions of graphene on (B-a – B-e) PatA, and (B-f – B-j) PatB. C) Optical images, Raman spectra, Raman I_D/I_G maps of graphene after reaction with 4-NBD on (C-a – C-c) PatA, and (C-d – C-f) PatB, (C-g) I_D/I_G profiles from (C-d) of graphene on PatB. Reproduced with permission.[129] Copyright 2020, Springer.

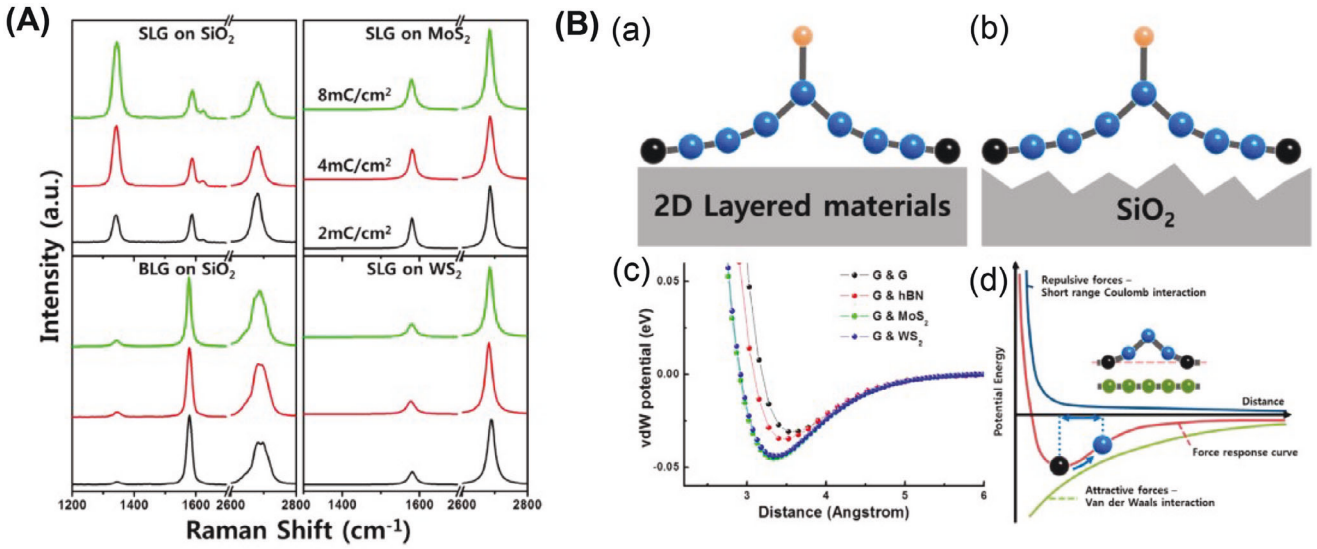

Figure 23. Reactivity of graphene supported on 2D materials. A) Raman spectra of SLG and BLG on different substrates after exposure to HSQ at different electron beam doses. B) Hydrogenated graphene on B-a) 2D substrate and B-a) SiO_2. B-c) vdW potential energy versus distance. B-d) Potential energy diagram of functionalized graphene on 2D substrate. Reproduced with permission.[31] Copyright 2015, American Chemical Society.

contrasting with the heavy doping observed in graphene on SiO_2 after similar treatment.[146] 2D materials as the substrates generally result in lower reactivity of graphene. For example, hBN lowered the reactivity of graphene toward radical addition,[125,127] thermal oxidation,[54] and hydrogenation by hydrogen plasma.[130] WS_2 and MoS_2 as the substrate decreased the reactivity of graphene toward hydrogenation by hydrogen silsesquioxane resist,[31] and antimonene as the substrate reduced the extent of graphene functionalization toward radical reaction.[131] One reported exception was MoS_2 toward hydrogenation by hydrogen plasma, which showed reactivity enhancement.[130,143]

Özyilmaz et al. studied hydrogenation and UVO oxidation of graphene, showing high chemical stability of graphene supported on vdW interactive 2D substrates such as WS_2, MoS_2, and h-BN.[31] The authors concluded that vdW interaction played a more dominant role in stabilizing graphene than local curvature effects or charge density inhomogeneity. Hydrogenation was carried out using hydrogen silsesquioxane (HSQ) and electron beam exposure. SLG on SiO_2 showed a dose-dependent increase in the D peak intensity, indicating high reactivity (**Figure 23**A). Under UVO treatment, SLG on SiO_2 was completely etched within minutes. In contrast, SLG and BLG on 2D substrates remained intact after UVO oxidation. After hydrogenation, graphene on MoS_2 and WS_2 showed almost no D peak at the highest electron beam dose, indicating minimal reactivity. Furthermore, vdW interactions facilitated dehydrogenation. Hydrogenated graphene transferred onto h-BN underwent substantial dehydrogenation, resulting in 16-fold decrease in I_D/I_G from 4.9 to 0.3. Theoretical simulations supported these findings, demonstrating that vdW interactions between graphene and 2D substrates (Figure 23B-c) generate a high resistive force that limits out-of-plane puckering and in-plane lattice deformation, thus lowering its chemical reactivity.

Son et al. investigated hydrogenation of graphene supported on MoS_2, h-BN and SiO_2 using 0.1 mbar hydrogen plasma (Ar/10% H_2).[130] The authors found that graphene on h-BN showed lower reactivity with 0.7% hydrogen coverage compared to ≈1.3% coverage on both SiO_2 and MoS_2. Raman mapping supported the reactivity difference. On MoS_2, the D peak, which was absent in pristine graphene, appeared at ≈1340 cm^{-1} after hydrogenation (**Figure 24**A). After hydrogenation, I_D/I_G was comparable for graphene on SiO_2 and MoS_2, indicating similar reactivity, whereas I_D/I_G for graphene on h-BN was about half of that of graphene on SiO_2, indicating lower reactivity (Figure 24B). The authors attributed the higher reactivity on MoS_2 to its ability to catalyze the hydrogenation reaction. For h-BN, the authors suggested that the vdW interaction between graphene and h-BN provides a resistive force that stabilizes the graphene lattice, thus reducing its reactivity.

Abellán et al. investigated how the interaction between graphene and the 2D material antimonene affected the reactivity of graphene toward radical reaction.[131] The sample was prepared by transferring CVD graphene onto hexagonal Sb nanosheets supported on silicon wafer (**Figure 25**A-a). Graphene on Sb showed a slight shift in the G peak, suggesting a possible charge interaction (Figure 25A-b). After functionalization with DBPO under laser irradiation (Figure 25B-a), graphene on Sb had a lower degree of functionalization compared to graphene on SiO_2, as seen by the reduced intensity of the D peak (Figure 25B-b). Bader charge transfer analysis revealed that the graphene-Sb interface was governed mainly by vdW forces rather than charge transfer. The calculated band structures showed that the Dirac cone of graphene on Sb remained intact, indicating minimal charge doping from Sb. Furthermore, the covalent functionalization was found to be reversible. Upon heating to 400 °C, the functional groups were removed, restoring the pristine graphene.

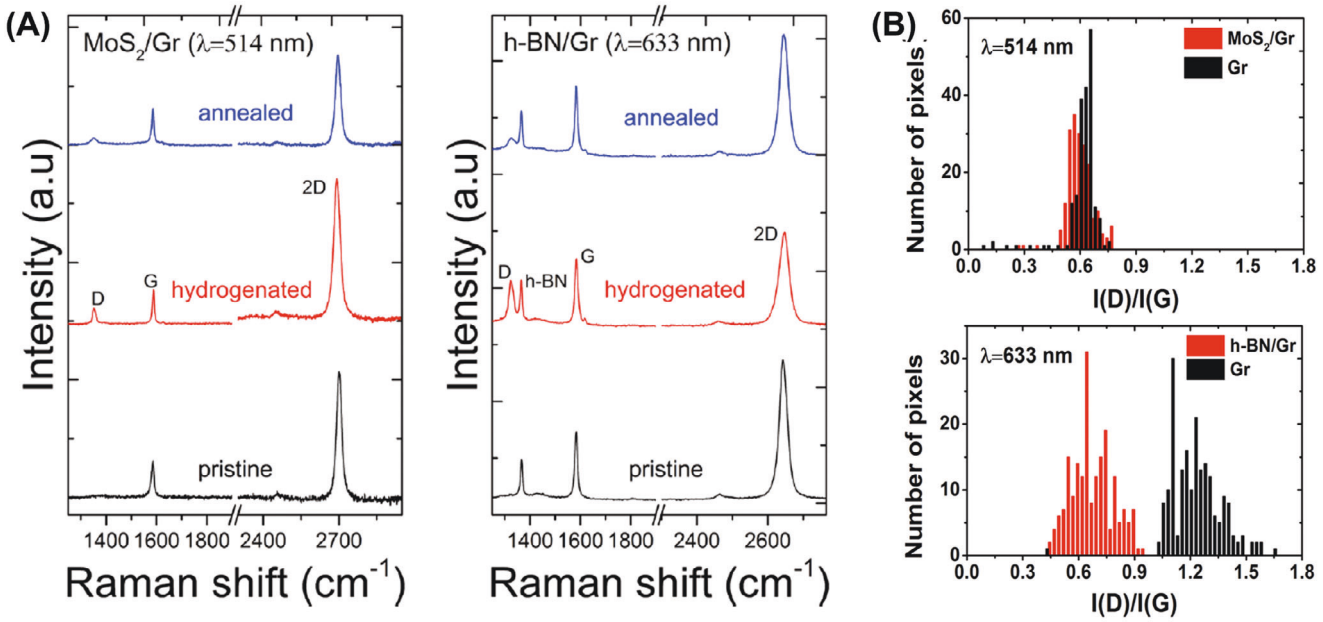

Figure 24. Hydrogenation of graphene supported on 2D materials. A) Raman spectra of pristine graphene, hydrogenated graphene, and annealed graphene on MoS_2 or h-BN. B) Histograms of I_D/I_G for hydrogenated graphene on MoS_2 or h-BN. Gr was graphene on SiO_2. Reproduced with permission.[130] Copyright 2016, AIP.

4. Conclusion and Prospect

Pristine graphene is a giant aromatic 2D material with limited chemical reactivity, mainly reacting with reactive species such as free radicals, carbenes and nitrenes, or under oxidative and reductive conditions. Methods that can enhance and control the reactivity of graphene is not only important to establish structure and reactivity relationship, but also for its practical applications in meeting technological challenges. In this context, substrate engineering has emerged as a powerful strategy in modulating the reactivity of graphene. In this review, we focus on the strain and charge doping from the supporting substrate and their effects on graphene reactivity. We discuss the origins of strain and charge doping, methods to characterize them, and provide examples of how these effects have been used to enhance the functionalization of graphene in various reactions.

Methods to introduce strain in graphene include using nanoparticle-decorated substrates, metal substrates with specific crystalline orientations, and stretchable polymers. On nanoparticle surfaces, curvatures induced by the conformal wrapping of graphene on the substrate create strains in graphene, leading to local deviations from its ideal planar structure. It was suggested that this strain is inversely related to nanoparticle size, with smaller nanoparticles creating higher strain. Examples reported to date have used different surface fabrication method and reaction conditions. Systematic studies that explore a broader

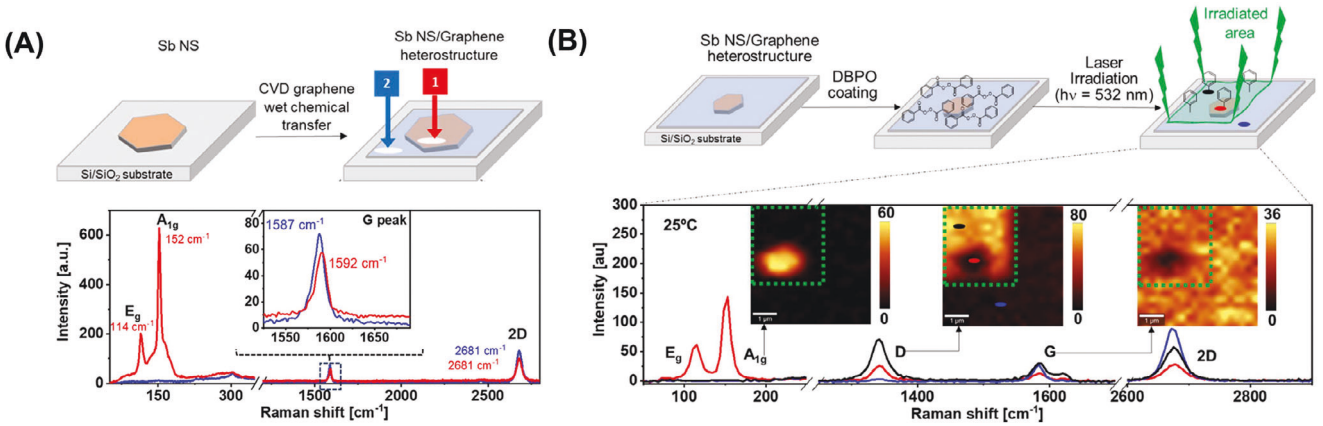

Figure 25. Radical reaction of graphene on Sb. A) Fabrication of graphene sample by transferring CVD graphene onto hexagonal Sb nanosheets (NS) supported on silicon wafer, and Raman spectra of graphene on Sb (red) and on SiO_2 (blue). B) Laser-induced free radical reaction of graphene with DBPO, and Raman spectra of functionalized graphene on Sb (red) and on SiO_2 (blue), and un-irradiated graphene (green). Reproduced with permission.[131] Copyright 2024, Royal Society of Chemistry.

range of nanoparticle sizes while maintaining the fabrication methods as well as reaction conditions consistent will help establish the relationship between nanoparticle size and graphene reactivity. The crystal orientation of metal substrates can influence the strain and thus the reactivity of graphene. Different metal orientations impose varying degrees of strain in graphene. For instance, CVD graphene grown on Cu(111) exhibits compressive strain during heating and cooling due to the mismatch in the thermal expansion coefficients between graphene and Cu(111). This has resulted in higher reactivity of graphene on Cu(111) compared to graphene on Cu(100) or *p*Cu in both a fluorination reaction[77] and radical reactions.[78,79] In an electrochemical reaction, higher reactivity of graphene was observed on Cu(115) than Cu(111).[119] A limitation of this approach is the availability and high cost of single-crystalline metal substrates. Deformation of polymer substrates is another effective way to introduce strain in graphene. The strain can be controlled by adjusting the extent of deformation of the polymer. Large deformation creates high density of wrinkles in graphene, which has shown enhanced reactivity toward fluorination[81] and radical reaction.[80] Note that the applied strain was measured by the extent of deformation of the polymer substrate, not the real strain in graphene in these cases.

Charge doping through substrates, including metals, oxides, and SAM-modified surfaces, has been effectively used to modulate the reactivity of graphene. The reactivity of graphene on metal substrates generally increases through orbital hybridization, charge transfer, and moiré patterns. For example, the strong orbital hybridization of graphene with Ni increases electron density on graphene, leading to high reactivity of graphene on Ni toward nitrene reactions.[113] Graphene on oxide substrates like SiO_2 and Al_2O_3 showed enhanced reactivity due to the formation of electron-hole puddles, leading to higher reactivity in electron transfer reactions such as the reactions with free radicals.[125,126] However, achieving uniform charge doping across the entire graphene sheet is challenging on oxide substrates due to inhomogeneous charge fluctuations. Graphene on 2D material substrates generally exhibits low reactivity due to the vdW interaction between the 2D material and graphene that stabilizes the graphene layer. One exception was reported for graphene supported on MoS_2, which showed high reactivity similar to graphene supported on SiO_2 in a hydrogenation reaction and was attributed to the catalytic activity of MoS_2.[130] Substrates functionalized with alkyl terminated SAMs usually reduce the effect of doping by screening surface charges, thus lowering the reactivity of graphene supported on these substrates.

A challenge in making quantitative comparisons of graphene reactivity across different results is the difficulty in isolating the effects of strain, charge doping, and other factors. Different preparation methods and conditions can produce graphene having varying degrees of strain and/or charge doping. For example, CVD graphene grown on Cu often shows p-type doping due to environmental exposure and residual chemicals during transfer. This is particularly true when using a polymer (e.g., poly(methyl methacrylate) for graphene transfer, which often leaves residues on graphene[147] and can contribute to unintentional doping. Also, studies have shown that the etchant solution can also induce significant compressive strain and p-doping in CVD graphene.[148] Therefore, developing standardized protocols to produce high-quality monolayer graphene free from unintended strain and doping will be highly desirable.

Also highly desirable are advanced techniques to characterize the precise molecular structure of graphene reaction products. Currently, the evaluations of graphene reactions primarily rely on Raman spectroscopy, particularly by comparing the Raman D band intensity and the I_D/I_G ratio, as seen in most examples discussed in this review. However, these Raman metrics do not give the exact molecular structure of the functionalized graphene product. Other methods such as XPS for elemental analysis and determining oxidation states, and AFM-based dynamic force measurements for mapping changes in the chemical functionality,[149] have been used. Again, these techniques do not give the precise molecular structure of the graphene product. Techniques that can offer structural details will provide a more accurate understanding of the reactions and the role of substrates in modulating the reactivity of graphene.

An exciting prospect of substrate engineering is its potential to selectively functionalize graphene, enabling precise control over the placement and density of functional groups. This allows for fine-tuning its electronic, chemical, and mechanical properties for applications in devices such as transistors and logic gates. Substrate engineering has proven valuable in achieving spatially controlled functionalization, as demonstrated in examples presented in this review, including the use of patterned substrates like LIPSS[129] and moiré patterns.[116–118] Tailoring vdW interaction strength between graphene and different substrates is another approach to selective functionalization, such as modifying high-doping regions on SiO_2 with Sb[131] or alkyl SAMs (e.g., OTS)[125] that screen charge doping. An emerging strategy involves using substrate curvatures to guide molecular migration on graphene, whereby covalently bonded molecules have been observed to migrate from positive curvature (valleys) to negative curvature (peaks), while non-covalently adsorbed molecules move from peaks to valleys.[150–152] This approach could potentially offer a novel way to modulate graphene reactivity by creating binding sites with tunable adsorption energies, facilitating selective functionalization and potentially dynamic reactivity through controlled adsorption and desorption.

Acknowledgements

The authors are grateful for the financial support from the National Science Foundation (CHE-2305006).

Conflict of Interest

The authors declare no conflict of interest.

Keywords

charge doping, graphene functionalization, strain, substrate engineering

Received: September 8, 2024
Revised: November 15, 2024
Published online:

[1] C. N. R. Rao, A. K. Sood, K. S. Subrahmanyam, A. Govindaraj, *Angew. Chem., Int. Ed.* **2009**, *48*, 7752.
[2] K. S. Kim, Y. Zhao, H. Jang, S. Y. Lee, J. M. Kim, K. S. Kim, J.-H. Ahn, P. Kim, J.-Y. Choi, B. H. Hong, *Nature* **2009**, *457*, 706.
[3] A. K. Geim, K. S. Novoselov, *Nat. Mater.* **2007**, *6*, 183.
[4] K. R. Nandanapalli, D. Mudusu, S. Lee, *Carbon* **2019**, *152*, 954.
[5] C. Wetzl, A. Silvestri, M. Garrido, H.-L. Hou, A. Criado, M. Prato, *Angew. Chem., Int. Ed.* **2023**, *62*, 202212857.
[6] L. Liao, H. Peng, Z. Liu, *J. Am. Chem. Soc.* **2014**, *136*, 12194.
[7] J. Park, M. Yan, *Acc. Chem. Res.* **2013**, *46*, 181.
[8] A. Kaplan, Z. Yuan, J. D. Benck, A. Govind Rajan, X. S. Chu, Q. H. Wang, M. S. Strano, *Chem. Soc. Rev.* **2017**, *46*, 4530.
[9] A. Stergiou, R. Cantón-Vitoria, M. N. Psarrou, S. P. Economopoulos, N. Tagmatarchis, *Prog. Mater. Sci.* **2020**, *114*, 100683.
[10] V. Georgakilas, M. Otyepka, A. B. Bourlinos, V. Chandra, N. Kim, K. C. Kemp, P. Hobza, R. Zboril, K. S. Kim, *Chem. Rev.* **2012**, *112*, 6156.
[11] J. Liu, J. Tang, J. J. Gooding, *J. Mater. Chem.* **2012**, *22*, 12435.
[12] E. Bekyarova, S. Sarkar, S. Niyogi, M. E. Itkis, R. C. Haddon, *J. Phys. D: Appl. Phys.* **2012**, *45*, 154009.
[13] E. Bekyarova, S. Sarkar, F. Wang, M. E. Itkis, I. Kalinina, X. Tian, R. C. Haddon, *Acc. Chem. Res.* **2013**, *46*, 65.
[14] S. Niyogi, E. Bekyarova, J. Hong, S. Khizroev, C. Berger, W. de Heer, R. C. Haddon, *J. Phys. Chem. Lett.* **2011**, *2*, 2487.
[15] S. Sarkar, E. Bekyarova, R. C. Haddon, *Mater. Today* **2012**, *15*, 276.
[16] T. S. Sreeprasad, V. Berry, *Small* **2013**, *9*, 341.
[17] M. A. Kim, N. Qiu, Z. Li, Q. Huang, Z. Chai, S. Du, H. Liu, *Adv. Funct. Mater.* **2020**, *30*, 1909269.
[18] R. Nouchi, *Nano Express* **2022**, *3*, 024001.
[19] C. M. Bazán, A. Béraud, M. Nguyen, A. Bencherif, R. Martel, D. Bouilly, *Nano Lett.* **2022**, *22*, 2635.
[20] S. Bian, A. M. Scott, Y. Cao, Y. Liang, S. Osuna, K. N. Houk, A. B. Braunschweig, *J. Am. Chem. Soc.* **2013**, *135*, 9240.
[21] L. Bao, B. Zhao, V. Lloret, M. Halik, F. Hauke, A. Hirsch, *Angew. Chem., Int. Ed.* **2020**, *59*, 6700.
[22] L. Bao, B. Zhao, M. Assebban, M. Halik, F. Hauke, A. Hirsch, *Chem.-Eur. J.* **2021**, *27*, 8709.
[23] R. A. Schäfer, K. Weber, M. Koleśnik-Gray, F. Hauke, V. Krstić, B. Meyer, A. Hirsch, *Angew. Chem., Int. Ed.* **2016**, *55*, 14858.
[24] J. Bai, X. Zhong, S. Jiang, Y. Huang, X. Duan, *Nat. Nanotechnol.* **2010**, *5*, 190.
[25] K. Chi, Z. Chen, F. Xiao, W. Guo, W. Xi, J. Liu, H. Yan, Z. Zhang, J. Xiao, J. Liu, J. Luo, S. Wang, K. P. Loh, *J. Mater. Chem. A* **2019**, *7*, 15575.
[26] Y. Lin, Y. Liao, Z. Chen, J. W. Connell, *Mater. Res. Lett.* **2017**, *5*, 209.
[27] W. Xia, J. Tang, J. Li, S. Zhang, K. C.-W. Wu, J. He, Y. Yamauchi, *Angew. Chem., Int. Ed.* **2019**, *58*, 13354.
[28] E. Celasco, G. Carraro, A. Lusuan, M. Smerieri, J. Pal, M. Rocca, L. Savio, L. Vattuone, *Phys. Chem. Chem. Phys.* **2016**, *18*, 18692.
[29] Y. Ding, Q. Peng, L. Gan, R. Wu, X. Ou, Q. Zhang, Z. Luo, *Chem. Mater.* **2016**, *28*, 1034.
[30] L. Liao, H. Wang, H. Peng, J. Yin, A. L. Koh, Y. Chen, Q. Xie, H. Peng, Z. Liu, *Nano Lett.* **2015**, *15*, 5585.
[31] J. H. Lee, A. Avsar, J. Jung, J. Y. Tan, K. Watanabe, T. Taniguchi, S. Natarajan, G. Eda, S. Adam, A. H. Castro Neto, *Nano Lett.* **2015**, *15*, 319.
[32] M. Biswal, X. Zhang, D. Schilter, T. K. Lee, D. Y. Hwang, M. Saxena, S. H. Lee, S. Chen, S. K. Kwak, C. W. Bielawski, W. S. Bacsa, R. S. Ruoff, *J. Am. Chem. Soc.* **2017**, *139*, 4202.
[33] F. M. Koehler, A. Jacobsen, K. Ensslin, C. Stampfer, W. J. Stark, *Small* **2010**, *6*, 1125.
[34] L. Liao, Z. Song, Y. Zhou, H. Wang, Q. Xie, H. Peng, Z. Liu, *Small* **2013**, *9*, 1348.
[35] L. Liu, S. Ryu, M. R. Tomasik, E. Stolyarova, N. Jung, M. S. Hybertsen, M. L. Steigerwald, L. E. Brus, G. W. Flynn, *Nano Lett.* **2008**, *8*, 1965.
[36] H. Liu, S. Ryu, Z. Chen, M. L. Steigerwald, C. Nuckolls, L. E. Brus, *J. Am. Chem. Soc.* **2009**, *131*, 17099.
[37] R. Sharma, J. H. Baik, C. J. Perera, M. S. Strano, *Nano Lett.* **2010**, *10*, 398.
[38] M. Ishigami, J.-H. Chen, W. G. Cullen, M. S. Fuhrer, E. D. Williams, *Nano Lett.* **2007**, *7*, 1643.
[39] G. Zhao, X. Li, M. Huang, Z. Zhen, Y. Zhong, Q. Chen, X. Zhao, Y. He, R. Hu, T. Yang, R. Zhang, C. Li, J. Kong, J.-B. Xu, R. S. Ruoff, H. Zhu, *Chem. Soc. Rev.* **2017**, *46*, 4417.
[40] E. Voloshina, Y. Dedkov, *Phys. Chem. Chem. Phys.* **2012**, *14*, 13502.
[41] M. Batzill, *Surf. Sci. Rep.* **2012**, *67*, 83.
[42] A. Dahal, M. Batzill, *Nanoscale* **2014**, *6*, 2548.
[43] A. Sinitskii, A. Dimiev, D. A. Corley, A. A. Fursina, D. V. Kosynkin, J. M. Tour, *ACS Nano* **2010**, *4*, 1949.
[44] J.-J. Lin, H.-F. Lv, X.-J. Wu, *Chin. J. Chem. Phys.* **2018**, *31*, 649.
[45] C. Morchutt, J. Björk, S. Krotzky, R. Gutzler, K. Kern, *Chem. Commun.* **2015**, *51*, 2440.
[46] H. Sung, M. Sharma, J. Jang, S.-Y. Lee, M.-g. Choi, K. Lee, N. Jung, *Nanoscale* **2019**, *11*, 5038.
[47] L. Zhu, W. Zhang, J. Zhu, D. Cheng, *Carbon* **2017**, *116*, 201.
[48] J. Hui, X. Zhou, R. Bhargava, A. Chinderle, J. Zhang, J. Rodríguez-López, *Electrochim. Acta.* **2016**, *211*, 1016.
[49] Y. Qu, Y. Ke, Y. Shao, W. Chen, C. T. Kwok, X. Shi, H. Pan, *J. Phys. Chem. C* **2018**, *122*, 25331.
[50] J. Park, T. Jin, C. Liu, G. Li, M. Yan, *ACS Omega* **2016**, *1*, 351.
[51] Z. H. Ni, T. Yu, Y. H. Lu, Y. Y. Wang, Y. P. Feng, Z. X. Shen, *ACS Nano* **2008**, *2*, 2301.
[52] H. Liu, Y. Liu, D. Zhu, *J. Mater. Chem.* **2011**, *21*, 3335.
[53] S. Park, D. Srivastava, K. Cho, *Nanotechnology* **2001**, *12*, 245.
[54] M. Yamamoto, T. L. Einstein, M. S. Fuhrer, W. G. Cullen, *ACS Nano* **2012**, *6*, 8335.
[55] T. Li, Z. Zhang, *J. Phys. D: Appl. Phys.* **2010**, *43*, 075303.
[56] S. R. Na, J. W. Suk, R. S. Ruoff, R. Huang, K. M. Liechti, *ACS Nano* **2014**, *8*, 11234.
[57] S. A. Campbell, *The Science and Engineering of Microelectronic Fabrication*, Oxford University Press, New York **1996**.
[58] W. G. Cullen, M. Yamamoto, K. M. Burson, J.-H. Chen, C. Jang, L. Li, M. S. Fuhrer, E. D. Williams, *Phys. Rev. Lett.* **2010**, *105*, 215504.
[59] J. E. Lee, G. Ahn, J. Shim, Y. S. Lee, S. Ryu, *Nat. Commun.* **2012**, *3*, 1024.
[60] H. Tomori, A. Kanda, H. Goto, Y. Ootuka, K. Tsukagoshi, S. Moriyama, E. Watanabe, D. Tsuya, *Appl. Phys. Express.* **2011**, *4*, 075102.
[61] G. Li, C. Yilmaz, X. An, S. Somu, S. Kar, Y. Joon Jung, A. Busnaina, K.-T. Wan, *J. Appl. Phys.* **2013**, *113*, 244303.
[62] A. Reserbat-Plantey, D. Kalita, Z. Han, L. Ferlazzo, S. Autier-Laurent, K. Komatsu, C. Li, R. Weil, A. Ralko, L. Marty, S. Guéron, N. Bendiab, H. Bouchiat, V. Bouchiat, *Nano Lett.* **2014**, *14*, 5044.
[63] B. Pacakova, T. Verhagen, M. Bousa, U. Hübner, J. Vejpravova, M. Kalbac, O. Frank, *Sci. Rep.* **2017**, *7*, 10003.
[64] J.-K. Lee, S. Yamazaki, H. Yun, J. Park, G. P. Kennedy, G.-T. Kim, O. Pietzsch, R. Wiesendanger, S. Lee, S. Hong, *Nano Lett.* **2013**, *13*, 3494.
[65] T. Hallam, A. Shakouri, E. Poliani, A. P. Rooney, I. Ivanov, A. Potie, H. K. Taylor, M. Bonn, D. Turchinovich, S. J. Haigh, J. Maultzsch, G. S. Duesberg, *Nano Lett.* **2015**, *15*, 857.
[66] O. Frank, G. Tsoukleri, J. Parthenios, K. Papagelis, I. Riaz, R. Jalil, K. S. Novoselov, C. Galiotis, *ACS Nano* **2010**, *4*, 3131.
[67] F. Ding, H. Ji, Y. Chen, A. Herklotz, K. Dörr, Y. Mei, A. Rastelli, O. G. Schmidt, *Nano Lett.* **2010**, *10*, 3453.
[68] T. M. G. Mohiuddin, A. Lombardo, R. R. Nair, A. Bonetti, G. Savini, R. Jalil, N. Bonini, D. M. Basko, C. Galiotis, N. Marzari, K. S. Novoselov, A. K. Geim, A. C. Ferrari, *Phys. Rev. B* **2009**, *79*, 205433.

[69] J. Zabel, R. R. Nair, A. Ott, T. Georgiou, A. K. Geim, K. S. Novoselov, C. Casiraghi, *Nano Lett.* **2012**, *12*, 617.
[70] C.-C. Chen, W. Bao, J. Theiss, C. Dames, C. N. Lau, S. B. Cronin, *Nano Lett.* **2009**, *9*, 4172.
[71] D. Yoon, Y.-W. Son, H. Cheong, *Nano Lett.* **2011**, *11*, 3227.
[72] T. Yu, Z. Ni, C. Du, Y. You, Y. Wang, Z. Shen, *J. Phys. Chem. C* **2008**, *112*, 12602.
[73] A. C. Ferrari, D. M. Basko, *Nat. Nanotechnol.* **2013**, *8*, 235.
[74] Q. Wu, Y. Wu, Y. Hao, J. Geng, M. Charlton, S. Chen, Y. Ren, H. Ji, H. Li, D. W. Boukhvalov, *Chem. Commun.* **2013**, *49*, 677.
[75] N. Hawthorne, S. Banerjee, Q. Moore, A. M. Rappe, J. D. Batteas, *J. Phys. Chem. C* **2022**, *126*, 17569.
[76] L. Zhou, L. Liao, J. Wang, J. Yu, D. Li, Q. Xie, Z. Liu, Y. Yang, X. Guo, Z. Liu, *Adv. Mater.* **2016**, *28*, 2148.
[77] J. Plšek, P. Kovaříček, V. Valeš, M. Kalbáč, *Chem.-Eur. J.* **2017**, *23*, 1839.
[78] B. W. Li, D. Luo, L. Zhu, X. Zhang, S. Jin, M. Huang, F. Ding, R. S. Ruoff, *Adv. Mater.* **2018**, *30*, 1706504.
[79] X. Zhang, D. Luo, H. Zhang, D. Y. Hwang, S. O. Park, B.-W. Li, M. Biswal, Y. Jiang, Y. Huang, S. K. Kwak, C. W. Bielawski, R. S. Ruoff, *Chem. Mater.* **2019**, *31*, 8639.
[80] M. A. Bissett, S. Konabe, S. Okada, M. Tsuji, H. Ago, *ACS Nano* **2013**, *7*, 10335.
[81] S. Deng, D. Rhee, W.-K. Lee, S. Che, B. Keisham, V. Berry, T. W. Odom, *Nano Lett.* **2019**, *19*, 5640.
[82] Z. Osváth, E. Gergely-Fülöp, N. Nagy, A. Deák, P. Nemes-Incze, X. Jin, C. Hwang, L. P. Biró, *Nanoscale* **2014**, *6*, 6030.
[83] Y. Zhang, M. Heiranian, B. Janicek, Z. Budrikis, S. Zapperi, P. Y. Huang, H. T. Johnson, N. R. Aluru, J. W. Lyding, N. Mason, *Nano Lett.* **2018**, *18*, 2098.
[84] B. Pacakova, J. Vejpravova, A. Repko, A. Mantlikova, M. Kalbac, *Carbon* **2015**, *95*, 573.
[85] M. Yamamoto, O. Pierre-Louis, J. Huang, M. S. Fuhrer, T. L. Einstein, W. G. Cullen, *Phys. Rev. X* **2012**, *2*, 041018.
[86] J. Vejpravova, B. Pacakova, J. Endres, A. Mantlikova, T. Verhagen, V. Vales, O. Frank, M. Kalbac, *Sci. Rep.* **2015**, *5*, 15061.
[87] J. C. Spear, J. P. Custer, J. D. Batteas, *Nanoscale* **2015**, *7*, 10021.
[88] O. Frank, J. Vejpravova, V. Holy, L. Kavan, M. Kalbac, *Carbon* **2014**, *68*, 440.
[89] J. H. Kang, J. Moon, D. J. Kim, Y. Kim, I. Jo, C. Jeon, J. Lee, B. H. Hong, *Nano Lett.* **2016**, *16*, 5993.
[90] V. Yu, E. Whiteway, J. Maassen, M. Hilke, *Phys. Rev. B* **2011**, *84*, 205407.
[91] M. Biswal, X. Zhang, D. Schilter, T. K. Lee, D. Y. Hwang, M. Saxena, S. H. Lee, S. Chen, S. K. Kwak, C. W. Bielawski, *J. Am. Chem. Soc.* **2017**, *139*, 4202.
[92] M. D. Huntington, C. J. Engel, T. W. Odom, *Angew. Chem., Int. Ed.* **2014**, *53*, 8117.
[93] W.-K. Lee, J. Kang, K.-S. Chen, C. J. Engel, W.-B. Jung, D. Rhee, M. C. Hersam, T. W. Odom, *Nano Lett.* **2016**, *16*, 7121.
[94] M. A. Bissett, M. Tsuji, H. Ago, *J. Phys. Chem. C* **2013**, *117*, 3152.
[95] R. J. Young, L. Gong, I. A. Kinloch, I. Riaz, R. Jalil, K. S. Novoselov, *ACS Nano* **2011**, *5*, 3079.
[96] M. A. Bissett, W. Izumida, R. Saito, H. Ago, *ACS Nano* **2012**, *6*, 10229.
[97] L. Gong, I. A. Kinloch, R. J. Young, I. Riaz, R. Jalil, K. S. Novoselov, *Adv. Mater.* **2010**, *22*, 2694.
[98] H. Lee, K. Paeng, I. S. Kim, *Synth. Met.* **2018**, *244*, 36.
[99] G. Giovannetti, P. A. Khomyakov, G. Brocks, V. v. Karpan, J. van den Brink, P. J. Kelly, *Phys. Rev. Lett.* **2008**, *101*, 026803.
[100] H. Pinto, R. Jones, J. Goss, P. Briddon, *Phys. Status Solidi A* **2010**, *207*, 2131.
[101] B. Guo, L. Fang, B. Zhang, J. R. Gong, *Insci. J.* **2011**, *1*, 80.
[102] C. Casiraghi, S. Pisana, K. Novoselov, A. K. Geim, A. Ferrari, *Appl. Phys. Lett.* **2007**, *91*, 233108.
[103] A. Das, S. Pisana, B. Chakraborty, S. Piscanec, S. K. Saha, U. V. Waghmare, K. S. Novoselov, H. R. Krishnamurthy, A. K. Geim, A. C. Ferrari, *Nat. Nanotechnol.* **2008**, *3*, 210.
[104] C. Casiraghi, *Phys. Rev. B* **2009**, *80*, 233407.
[105] D. Basko, S. Piscanec, A. Ferrari, *Phys. Rev. B* **2009**, *80*, 165413.
[106] L. Kong, C. Bjelkevig, S. Gaddam, M. Zhou, Y. H. Lee, G. H. Han, H. K. Jeong, N. Wu, Z. Zhang, J. Xiao, P. A. Dowben, J. A. Kelber, *J. Phys. Chem. C* **2010**, *114*, 21618.
[107] M. S. Jagadeesh, A. Calloni, G. Bussetti, L. Duò, F. Ciccacci, *Phys. Status Solidi B* **2018**, *255*, 1700415.
[108] Y. Dedkov, E. Voloshina, *J. Phys.: Condens. Matter.* **2015**, *27*, 303002.
[109] Y. S. Dedkov, M. Fonin, *New J. Phys.* **2010**, *12*, 125004.
[110] J. Wintterlin, M.-L. Bocquet, *Surf. Sci.* **2009**, *603*, 1841.
[111] C. J. Chen, *Introduction to Scanning Tunneling Microscopy*, 3rd ed., Oxford University Press, USA **2021**.
[112] M. Smerieri, E. Celasco, G. Carraro, A. Lusuan, J. Pal, G. Bracco, M. Rocca, L. Savio, L. Vattuone, *ChemCatChem* **2015**, *7*, 2328.
[113] X. Yang, F. Chen, M. A. Kim, H. Liu, L. M. Wolf, M. Yan, *Chem. - Eur. J.* **2021**, *27*, 7887.
[114] X. Yang, F. Chen, M. A. Kim, H. Liu, L. M. Wolf, M. Yan, *Phys. Chem. Chem. Phys.* **2022**, *24*, 20082.
[115] T. Zhang, S. B. Khomane, I. Singh, C. M. Crudden, P. H. McBreen, *J. Phys. Chem. C* **2022**, *126*, 14430.
[116] R. Balog, B. Jørgensen, L. Nilsson, M. Andersen, E. Rienks, M. Bianchi, M. Fanetti, E. Lægsgaard, A. Baraldi, S. Lizzit, *Nat. Mater.* **2010**, *9*, 315.
[117] S. J. Altenburg, M. Lattelais, B. Wang, M.-L. Bocquet, R. Berndt, *J. Am. Chem. Soc.* **2015**, *137*, 9452.
[118] J. J. Navarro, S. Leret, F. Calleja, D. Stradi, A. Black, R. Bernardo-Gavito, M. Garnica, D. Granados, A. L. Vázquez de Parga, E. M. Pérez, R. Miranda, *Nano Lett.* **2016**, *16*, 355.
[119] M. Kim, S. H. Joo, M. Wang, S. G. Menabde, D. Luo, S. Jin, H. Kim, W. K. Seong, M. S. Jang, S. K. Kwak, S. H. Lee, R. S. Ruoff, *ACS Nano* **2023**, *17*, 18914.
[120] G. J. Shenoy, D. Parobek, M. Salim, Z. Li, C. Tian, H. Liu, *RSC Adv.* **2016**, *6*, 8489.
[121] Z. Li, F. Zhou, D. Parobek, G. J. Shenoy, P. Muldoon, H. Liu, *J. Solid State Chem.* **2015**, *224*, 14.
[122] A. Ambrosetti, P. L. Silvestrelli, *J. Chem. Phys.* **2016**, *144*, 111101.
[123] E. Celasco, G. Carraro, M. Smerieri, L. Savio, M. Rocca, L. Vattuone, *J. Chem. Phys.* **2017**, *146*, 104704.
[124] P. Sutter, J. T. Sadowski, E. A. Sutter, *J. Am. Chem. Soc.* **2010**, *132*, 8175.
[125] Q. H. Wang, Z. Jin, K. K. Kim, A. J. Hilmer, G. L. Paulus, C.-J. Shih, M.-H. Ham, J. D. Sanchez-Yamagishi, K. Watanabe, T. Taniguchi, *Nat. Chem.* **2012**, *4*, 724.
[126] X. Fan, R. Nouchi, K. Tanigaki, *J. Phys. Chem. C* **2011**, *115*, 12960.
[127] G. Gao, D. Liu, S. Tang, C. Huang, M. He, Y. Guo, X. Sun, B. Gao, *Sci. Rep.* **2016**, *6*, 20034.
[128] Y. K. Lee, H. Choi, C. Lee, H. Lee, K. C. Goddeti, S. Y. Moon, W. H. Doh, J. Baik, J.-S. Kim, J. S. Choi, *Nanoscale* **2016**, *8*, 11494.
[129] K. A. Drogowska-Horna, I. Mirza, A. Rodriguez, P. Kovaříček, J. Sládek, T. J.-Y. Derrien, M. Gedvilas, G. Račiukaitis, O. Frank, N. M. Bulgakova, *Nano Res.* **2020**, *13*, 2332.
[130] S. Son, C. Holroyd, J. Clough, A. Horn, S. P. K. Koehler, C. Casiraghi, *Appl. Phys. Lett.* **2016**, *109*, 243103.
[131] M. Fickert, R. Martinez-Haya, A. Ruiz, J. Baldoví, G. Abellán, *RSC Adv.* **2024**, *14*, 13758.
[132] E. H. Hwang, S. Adam, S. D. Sarma, *Phys. Rev. Lett.* **2007**, *98*, 186806.
[133] J. H. Chen, C. Jang, S. Adam, M. S. Fuhrer, E. D. Williams, M. Ishigami, *Nat. Phys.* **2008**, *4*, 377.

[134] J. Martin, N. Akerman, G. Ulbricht, T. Lohmann, J. H. Smet, K. von Klitzing, A. Yacoby, *Nat. Phys.* **2008**, *4*, 144.
[135] Y. Zhang, V. W. Brar, C. Girit, A. Zettl, M. F. Crommie, *Nat. Phys.* **2009**, *5*, 722.
[136] B. I. Shklovskii, *Phys. Rev. B* **2007**, *76*, 233411.
[137] V. M. Galitski, S. Adam, S. Das Sarma, *Phys. Rev. B* **2007**, *76*, 245405.
[138] T. Tsukamoto, K. Yamazaki, H. Komurasaki, T. Ogino, *J. Phys. Chem. C* **2012**, *116*, 4732.
[139] J. Shim, C. H. Lui, T. Y. Ko, Y.-J. Yu, P. Kim, T. F. Heinz, S. Ryu, *Nano Lett.* **2012**, *12*, 648.
[140] Z. Yan, Z. Sun, W. Lu, J. Yao, Y. Zhu, J. M. Tour, *ACS Nano* **2011**, *5*, 1535.
[141] M. Lafkioti, B. Krauss, T. Lohmann, U. Zschieschang, H. Klauk, K. v. Klitzing, J. H. Smet, *Nano Lett.* **2010**, *10*, 1149.
[142] K. Yokota, K. Takai, T. Enoki, *Nano Lett.* **2011**, *11*, 3669.
[143] A. K. Geim, I. V. Grigorieva, *Nature* **2013**, *499*, 419.
[144] C. Li, Q. Cao, F. Wang, Y. Xiao, Y. Li, J.-J. Delaunay, H. Zhu, *Chem. Soc. Rev.* **2018**, *47*, 4981.
[145] J. Xue, J. Sanchez-Yamagishi, D. Bulmash, P. Jacquod, A. Deshpande, K. Watanabe, T. Taniguchi, P. Jarillo-Herrero, B. J. LeRoy, *Nat. Mater.* **2011**, *10*, 282.
[146] C. R. Dean, A. F. Young, I. Meric, C. Lee, L. Wang, S. Sorgenfrei, K. Watanabe, T. Taniguchi, P. Kim, K. L. Shepard, J. Hone, *Nat. Nanotechnol.* **2010**, *5*, 722.
[147] X. Yang, M. Yan, *Nano Res.* **2020**, *13*, 599.
[148] Z. Wu, X. Zhang, A. Das, J. Liu, Z. Zou, Z. Zhang, Y. Xia, P. Zhao, H. Wang, *RSC Adv.* **2019**, *9*, 41447.
[149] J. P. Froning, P. Lazar, M. Pykal, Q. Li, M. Dong, R. Zbořil, M. Otyepka, *Nanoscale* **2017**, *9*, 119.
[150] S. Banerjee, A. M. Rappe, *J. Am. Chem. Soc.* **2022**, *144*, 7181.
[151] M. He, T. M. Swager, *J. Am. Chem. Soc.* **2020**, *142*, 17876.
[152] S. Banerjee, N. Hawthorne, J. D. Batteas, A. M. Rappe, *J. Am. Chem. Soc.* **2023**, *145*, 26765.

Jia Tu is a Ph.D. student in the laboratory of Prof. Yan at the Chemistry Department, University of Massachusetts Lowell. He received his B.S. degree in applied chemistry from Northwest A&F University, and M.S. degree in polymer chemistry and physics from Beijing Normal University. His research focus is on the chemistry of graphene.

Mingdi Yan is a chemistry professor at the University of Massachusetts Lowell. She obtained a B.S. from the University of Science and Technology of China and a Ph.D. from the University of Oregon. Her research interests include the chemical functionalization of graphene, graphene-based composite materials, and biointerface chemistry. She has published extensively on the photochemical and cycloadditions of electrophilic aryl azides, as well as the applications in materials chemistry and chemical biology.